Journal of Computational Physics 229 (2010) 6744–6780

Contents lists available at ScienceDirect

Journal of Computational Physics

journal homepage: www.elsevier.com/locate/jcp

On high-order shock-fitting and front-tracking schemes for numerical simulation of shock–disturbance interactions

Pradeep Singh Rawat *, Xiaolin Zhong

Mechanical and Aerospace Engineering Department, University of California, Los Angeles, CA 90095-1597, United States

ARTICLE INFO

Article history:
Received 24 June 2009
Received in revised form 15 May 2010
Accepted 18 May 2010
Available online 31 May 2010

Keywords:
Shock-fitting methods
High-order finite-difference schemes
Shock–turbulence interaction

ABSTRACT

High-order methods that can resolve interactions of flow-disturbances with shock waves are critical for reliable numerical simulation of shock wave and turbulence interaction. Such problems are not well understood due to the limitations of numerical methods. Most of the popular shock-capturing methods are only first-order accurate at the shock and may incur spurious numerical oscillations near the shock. Shock-fitting algorithms have been proposed as an alternative which can achieve uniform high-order accuracy and can avoid possible spurious oscillations incurred in shock-capturing methods by treating shocks as sharp interfaces. We explore two ways for shock-fitting: conventional moving grid set-up and a new fixed grid set-up with front tracking. In the conventional shock-fitting method, a moving grid is fitted to the shock whereas in the newly developed fixed grid set-up the shock front is tracked using Lagrangian points and is free to move across the underlying fixed grid. Different implementations of shock-fitting methods have been published in the literature. However, uniform high-order accuracy of various shock-fitting methods has not been systematically established. In this paper, we carry out a rigorous grid-convergence analysis on different variations of shock-fitting methods with both moving and fixed grids. These shock-fitting methods consist of different combinations of numerical methods for computing flow away from the shock and those for computing the shock movement. Specifically, we consider fifth-order upwind finite-difference scheme and shock-capturing WENO schemes with conventional shock-fitting and show that a fifth-order convergence is indeed achieved for a canonical one-dimensional shock-entropy wave interaction problem. We also show that the method of finding shock velocity from one characteristic relation and Rankine–Hugoniot jump condition performs better than the other methods of computing shock velocities. A high-order front-tracking implementation of shock-fitting is also presented in this paper and nominal rate of convergence is shown. The front-tracking results are validated by comparing to results from the conventional shock-fitting method and a linear-interaction analysis for a two-dimensional shock disturbance interaction problem.

1. Introduction

Complex interactions between turbulent flows and shock waves are observed in several processes such as volcanic eruptions, detonations, supernova explosion and many aerodynamic applications. Numerical simulation of such complex problems warrants very high-order numerical methods. High-order shock-capturing schemes have been the methods of choice in most previous numerical simulation studies of shock–turbulence interaction [1–4]. However, popular shock-capturing

* Corresponding author. Tel.: +1 310 825 2905.
E-mail address: pradeep@seas.ucla.edu (P.S. Rawat).

0021-9991/$ - see front matter © 2010 Elsevier Inc. All rights reserved.
doi:10.1016/j.jcp.2010.05.021

schemes reduce to first-order accuracy near the shock due to the use of dissipation near the shock. Moreover, spurious numerical oscillations have been observed when solving strong-shock and flow interaction problems with shock-capturing schemes [5]. In the present study, we investigate shock-fitting algorithms for shock and disturbance interaction studies. Problem of interaction of normal shock and disturbances is fundamental to better understanding of the aforementioned complex phenomena. To this end, shock-fitting methods developed in the current effort can be useful to find high-order solutions of some simple shock and turbulence interaction problems such as shown in Fig. 1. Various researchers have considered such shock and disturbance/turbulence interaction problems in past. A brief summary is presented in ensuing sections for previous works in the field, followed by the scope of current study.

1.1. Theoretical studies

Theoretical studies in the field of shock–turbulence interaction have been attempted mostly through linear interaction analysis (LIA), where small perturbations in flow are considered. Kovasznay [6] showed that for weak fluctuations of velocity, pressure, and entropy, the turbulent fluctuations about mean uniform flow can be decomposed into the vorticity, acoustic, and entropy modes. It was shown that for first-order approximation, each of these modes evolve independently in the inviscid limit. However, in second-order approximation of fluctuations, interaction of these modes is possible and any two modes can combine to generate other modes [7].

Ribner [8–10] and Moore [11] were among the earliest workers to consider theoretically the interaction of a turbulent field with a shock wave. Ribner [8] analyzed the interaction of a plane sinusoidal disturbance in velocity (shear wave) passing through a shock as a boundary-value problem. In his analysis, the shock was kept steady by solving the equations in a moving reference frame. It was found that the initial shear wave is amplified and refracted by the shock. He later generalized this result from a single wave to obtain shock-interaction effects of a completely turbulent velocity field [9] and reported significant turbulent amplification due to shock–turbulence interaction. The results were further extended [10] to provide the flux of acoustic energy emanating from a unit area downstream of the shock. Moore [11] performed unsteady analysis of interaction of obliquely traveling weak plane disturbances of arbitrary profile with a plane normal shock. Unlike Ribner's analysis, an unsteady shock was considered for linear analysis of the interaction of sound and vorticity waves with an unsteady shock. It was found that amplification of disturbances depends on impingement angle and Mach number of the shock. Kerrebrock [12] considered modifications of random small fluctuations of pressure, entropy and vorticity in passing through a shock wave or flame. It was found that all modes of disturbances are generated in the downstream flow if any of the modes is present in the upstream flow. McKenzie and Westphal [13] derived formulas for amplification and Snell's Laws for refraction and reflection of acoustic, vorticity, and entropy waves interacting with a shock and applied the results to the amplification of small disturbances in the solar wind on a passage through the bow shock of earth. More recent theoretical studies of shock and turbulence interaction are by Goldstein [14], Lee et al. [15–17], Mahesh et al. [2,3,18] and Fabre et al. [19]. These studies found that root mean square values of the fluctuating pressure, temperature, density, and different components of the turbulent kinetic energy, are amplified across the shocks. Despite several assumptions, linear-interaction analysis (LIA) accurately describes the essential characteristics of the interaction.

1.2. Numerical studies

Since the early 1980s, various attempts have been made towards direct numerical simulation of shock and disturbance/turbulence interaction. Initial efforts in this area considered the interaction of a shock with simple waves. In 1981, Pao and Salas [20] fitted the shock at an inflow boundary and solved the Euler equation with finite-difference discretization to study a shock/vortex interaction. Shock-fitting computations with spectral techniques (Hussaini et al. [21,22], Zang et al. [23]) were later used to treat the problems in which a single vortex, a vortex sheet, an entropy spot, or an acoustic wave interacts with the shock. The results obtained from these numerical efforts confirmed the linear theory in the regime of weak shocks. With the advent of essentially non-oscillatory (ENO) and related schemes, shock-capturing methods gained popularity for simulations of compressible flows. A number of new shock-capturing schemes for compressible flows have since been tested for interaction of a shock wave with small disturbances against the results obtained from linear theory [22,24,25]. Although limited to low Mach numbers, these studies mostly confirm the LIA results.

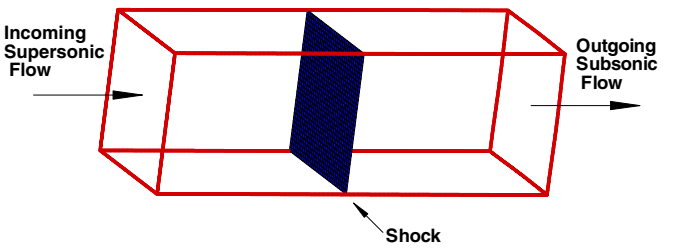

Fig. 1. A schematic of typical setting of isotropic shock and turbulence interaction.

The direct numerical studies of a fully turbulent field interacting with shocks are more recent. For the simulation of the turbulent field, direct numerical simulation (DNS) methods and large eddy simulations (LES) have been used. However, these different types of methods give different results when interaction with a shock is considered [26]. Most of the recent DNS studies have been on various aspects of the interaction of a normal shock with free-stream turbulence for a relatively weak shock of small Mach numbers. For example, Mahesh et al. [2,3] did an extensive DNS study of the interaction of a normal shock with an isotropic turbulence. The mean shock Mach numbers were in the range of 1.29–1.8. They found that the upstream correlation between the vorticity and entropy fluctuations has strong influence on the evolution of turbulence across the shock. They also used linear analysis to analyze the simulation results. Other shock–turbulence interaction studies have been conducted by the same group of workers [15,16]. Lee et al. [16] investigated the effect of Mach numbers on isotropic turbulence interacting with a shock wave. The Mach numbers ranged from 1.5 to 3.0. A shock-capturing scheme was developed to accurately simulate the unsteady interaction of turbulence with shock waves. It was found that turbulent kinetic energy is amplified across the shock wave, and this amplification tends to saturate beyond Mach 3. Hannappel et al. [27] computed interaction of a Mach 2 shock with a third-order shock-capturing scheme based on the essentially non-oscillatory (ENO) algorithm of Harten. Jamme et al. [28] carried out a DNS study of the interaction between normal shock waves of moderate strength (Mach 1.2 and Mach 1.5) and isotropic turbulence. Adams and Shariff [29,30] proposed a class of upwind-biased finite-difference schemes with a compact stencil for shock–turbulence interaction simulation. They used this non-conservative upwind scheme in smooth regions while a shock-capturing ENO scheme was turned on around discontinuities. This idea of hybrid formulation was improved by Pirozzoli [31], who used a similar hybrid formulation for a compact weighted essentially non-oscillatory (WENO) scheme with conservative formulation for simulation of shock–turbulence interaction. Ducros et al. [32] conducted larger-eddy simulation on shock–turbulence interaction by using a second-order finite volume scheme. The method was then used to simulate the interaction of a Mach 1.2 shock with homogeneous turbulence.

Yee et al. [33] proposed a new kind of characteristic-type filters, which add the dissipative part of traditional shock-capturing schemes to non-dissipative central schemes in order to damp out numerical instabilities. Due to this feature, characteristic filters are suitable for incorporation into existing LES codes based on high-order methods, and they allow the codes to have shock-capturing capability. This scheme was used by Sjogreen and Yee [34] for shock disturbance interaction. Recently, Cook and Cabot [35] have used hyperviscosity formulations for shock–turbulence simulations. It functions as an effective subgrid-scale model for both high and low Mach number flows. The model employs a bulk viscosity for treating shocks and a shear viscosity for treating turbulence and has been used for the basic shock disturbance interaction.

It is observed that most of the studies in the field of shock–turbulence interaction have considered weak shocks only. Recently, more efforts have been directed towards investigating turbulent flows with stronger shocks, which is relevant for high-speed compressible flows. One of the main issues with shock-capturing schemes is spurious numerical oscillations created around the shock and the loss of accuracy with dissipation needed to suppress these oscillations. Recently, Sesterhenn et al. [36] revisited shock-fitting schemes and applied them for solving the Navier–Stokes equations in non-conservative form for the problem of interaction of a Mach 3 shock with isotropic turbulence with encouraging results. The shock-fitting method offers a good alternative for strong shocks with simple geometries as the shock wave is considered a sharp discontinuity.

1.3. Shock-fitting methods

Shock-fitting schemes have been used for simulations of compressible flow with well-defined shocks since the 1960s. Moretti and collaborators developed efficient and reliable codes using shock-fitting for steady and time-dependent flows [37–40]. In order to compute shock velocities, the Rankine–Hugoniot (R–H) conditions were used with a compatibility equation along a generator of the characteristic conoid reaching the shock. A modification of the method was proposed by Kentzer [41] and later by de Neef and Moretti [42], where temporal derivatives of the Rankine–Hugoniot conditions were used with characteristic equations to find the shock velocity. Since such flows do not need any shock capturing, conservative forms of the governing equations were not required. Moretti used Riemann's characteristic equations, discretizing them based on the direction of propagation of the associated waves. Such methods were named λ-schemes [43] and were used exclusively with the shock-fitting method [44–48]. Moretti also considered multi-dimensional flows where shocks are not aligned with any grid lines but float across the grids [49]. Further work was done on this floating shock-fitting technique to make it simpler [50,51]. However, topological problems were encountered if more than one shock were present. A review of the development of the shock-fitting methods can be found in Refs. [52,53].

Original shock-fitting schemes, with grids aligned with the shock, were adopted by a number of researchers. In the 1990's shock-fitting was used mostly for solving flow over blunt bodies. The bow shocks were treated as a computational boundary. Pseudo-spectral approximations to the Euler equations employing shock-fitting were first performed by Hussaini et al. [21]. Kopriva [54,55] used the Chebyshev spectral collocation method in conjunction with shock-fitting and extended it to multidomain [56]. Cai [57] used a shock-fitting algorithm to compute two-dimensional detonation waves. Zhong [58] developed new high-order finite-difference schemes and coupled them with the shock-fitting algorithm for studying hypersonic boundary layers. These schemes were used for receptivity studies of supersonic boundary layers [59–63]. Brooks and Powers [64] extended Kopriva's spectral method with shock-fitting to solve two-dimensional axisymmetric Euler equations in a cylindrical coordinate frame for blunt body problems. Recently, Mahlmann et al. [65] used Chebyshev spectral collocation with shock-fitting method for study of effects of free-stream disturbances in the leading-edge region of a blunt flat plate in supersonic flow.

As discussed earlier, the shock-fitting method has also been applied to problems of shock and disturbance interactions. Sesterhenn et al. [19,36] decomposed the inviscid part of the threedimensional Navier–Stokes equations in characteristic (acoustic and convective) waves aligned with the numerical grid. Variables representing these characteristic waves are discretized using a compact fifth-order upwind scheme. This method is an extension of Moretti's λ-schemes and has been validated for the problems of shock and entropy spot interaction and shock and isotropic turbulence interaction. This scheme is different from the shock-fitting scheme we are using [58]. We solve the Navier–Stokes equation in conservative form as opposed to the non-conservative formulation used by Sesterhenn et al. [36] since it enables us to capture weak discontinuities behind the main shock.

Shock-fitting methods consider the shock as a sharp discontinuity and there is no numerical smearing of the shock fronts. Compared to shock capturing methods, the main advantage of shock-fitting methods is the possibility of achieving uniform high-order accuracy for flow containing shock waves and avoiding possible spurious oscillations. On the contrary, most of the popular shock-capturing methods are only first-order accurate at the shock and may incur spurious numerical oscillations near the shock.

1.4. Motivation and scope of current study

The preceding review of the field of shock interactions with disturbances and turbulence shows that the current scientific understanding of shock–turbulence interactions in complex configurations and the ability to reliably predict these strongly nonlinear flows remains limited. Most of the popular methods for solving compressible flow involve shock-capturing algorithms for treatment of shocks. However, it has been observed that even high-order shock-capturing methods give low accuracy in the vicinity of the shock [66] and may lead to spurious oscillations [5]. Many shock-capturing methods introduce some dissipation to avoid spurious oscillations which, however, is not accurate enough for simulation of turbulent flow. On the other hand, conventional high-order finite-difference schemes or spectral methods generally used for DNS studies cannot resolve strong gradients around shocks due to numerical instability.

In the present study, we develop shock-fitting algorithms along with high-order finite-difference schemes to gain knowledge about nonlinear phenomena involving interaction of strong shocks and flow disturbances. Shock-fitting algorithms treat the shock-interface sharply without local reduction of order of accuracy and are therefore compatible with low dissipation high-order schemes used for DNS of turbulent flow. Shock/interface fitting methods are ideally suited for the cases where there is a clearly demarcated interface, such as observed in the problems involving disturbances coming towards the normal shock. Some of canonical problems in one and two-dimensional space have been considered in this paper and the obtained results point to the superior performance of the shock-fitting methods for such problems.

Conventionally, a shock is treated as a boundary in shock-fitting methods and grids follow the shock during the computations. This, however, might not be feasible if the shock shape becomes complex or there are large movements in the shock. For such situations, it is useful to extend the high-order shock-fitting idea for implementation with fixed grids where the shock front moves across grid lines. Hence, an aim of the current study is to develop new methods and algorithms to use idea of shock-fitting on fixed grids with the help of a front-tracking method. We have developed a 2-D algorithm based on the front-tracking approach where we use Lagrangian type marker points to track the shock front. Shock velocity is obtained from a shock acceleration equation following the shock-fitting method used by Zhong [58]. The method is described in Section 4 and results for one and two-dimensional shock–disturbance problems are presented in Section 7.

Several different ways to implement the shock-fitting methods exist in the literature. However, uniform high-order accuracy of various shock-fitting methods has not been systematically established for most of these methods. In this paper, we carry out a rigorous grid-convergence study of seven different conventional shock-fitting methods for shock–disturbance interaction problems. These seven shock-fitting methods consist of different combinations of numerical methods for computing flow away from the shock and those for computing the shock velocities.

A convergence study for unsteady shock–disturbance interaction problem computed by the shock-fitting algorithms is presented in Section 5. A two-dimensional shock–disturbance interaction problem is then considered with shock-fitting and results are compared with those from the literature in Section 6.

Thus, main focus of the current paper is identifying various aspects of the shock-fitting algorithm that will lead to truly high-order solutions for problems involving unsteady shock and flow interactions. Although the conventional shock-fitting schemes can be used for only simple geometries, they offer the accuracy which can not be achieved by the common shock-capturing schemes. Shock-fitting has been found to be very useful for many problems which involve simple shock geometry but complex flow physics. Examples of these problems include shock–turbulence interaction [36], receptivity of hypersonic boundary layer to free-stream disturbances [62,67] and detonations [57,68]. Moreover, the paper demonstrates high-order accuracy for conventional as well as front tracking implementation of the shock-fitting, which provides motivation for further development of shock-fitting based algorithms for more complex problems.

2. Governing equations

The general governing equations for compressible flow considered in this paper are the Euler equations which are given as follows:

$$\frac{\partial \rho}{\partial t} + \nabla \cdot (\rho \mathbf{u}) = 0 \tag{1}$$

$$\rho\left(\frac{\partial \mathbf{u}}{\partial t} + \mathbf{u} \cdot \nabla \mathbf{u}\right) = -\nabla p \tag{2}$$

$$\frac{\partial e}{\partial t} + \nabla \cdot (e\mathbf{u}) = -\nabla \cdot (p\mathbf{u}) \tag{3}$$

where ρ and p represent density and pressure, respectively. $\mathbf{u} = u\hat{i} + v\hat{j} + w\hat{k}$ is the velocity vector and $e = p/(\gamma - 1) + \rho(u^2 + v^2 + w^2)/2$ is the total energy of the fluid.

In numerical simulations, the compressible Euler equations (1)–(3) are written in the following conservative form,

$$\frac{\partial \mathbf{U}}{\partial t} + \frac{\partial \mathbf{E}}{\partial x} + \frac{\partial \mathbf{F}}{\partial y} + \frac{\partial \mathbf{G}}{\partial z} = 0 \tag{4}$$

where U is the solution vector given by

$$\mathbf{U} = \{\rho, \rho u, \rho v, \rho w, e\} \tag{5}$$

E, F, G are the inviscid flux terms. They are written as follows:

$$\mathbf{E} = \begin{Bmatrix} \rho u \\ \rho u^2 + p \\ \rho u v \\ \rho u w \\ (e + p)u \end{Bmatrix} \tag{6}$$

$$\mathbf{F} = \begin{Bmatrix} \rho v \\ \rho v u \\ \rho v^2 + p \\ \rho v w \\ (e + p)v \end{Bmatrix} \tag{7}$$

$$\mathbf{G} = \begin{Bmatrix} \rho w \\ \rho w u \\ \rho w v \\ \rho w^2 + p \\ (e + p)w \end{Bmatrix} \tag{8}$$

3. High-order moving-grid shock-fitting method

In conventional moving-grid shock-fitting approach, a shock wave is taken as a boundary of the computational domain. Before discretizing the governing equations by a finite-difference method, Eq. (4) in the physical domain is transformed to the shock and boundary fitted computational domain by the following transformation relations,

$$\begin{cases} \xi = \xi(x, y, z) \\ \eta = \eta(x, y, z) \\ \varsigma = \varsigma(x, y, z) \\ \tau = t \end{cases} \Longleftrightarrow \begin{cases} x = x(\xi, \eta, \varsigma, \tau) \\ y = y(\xi, \eta, \varsigma, \tau) \\ z = z(\xi, \eta, \varsigma, \tau) \\ t = \tau \end{cases} \tag{9}$$

and the transformed governing equation in the computational domain is expressed as follows:

$$\frac{1}{J}\frac{\partial U}{\partial \tau} + \frac{\partial E'}{\partial \xi} + \frac{\partial F'}{\partial \eta} + \frac{\partial G'}{\partial \zeta} + U\frac{\partial}{\partial \tau}\left(\frac{1}{J}\right) = 0 \tag{10}$$

where

$$\begin{aligned} E' &= \frac{E\xi_x + F\xi_y + G\xi_z}{J} \\ F' &= \frac{E\eta_x + F\eta_y + G\eta_z + U\eta_t}{J} \\ G' &= \frac{E\zeta_x + F\zeta_y + G\zeta_z}{J} \end{aligned} \tag{11}$$

Here, J is the Jacobian of the coordinate transformation. All grid transformation metrics can be computed as a function of distance of shock front from the exit boundary along η grid line, $H(\xi,\eta,\zeta)$, and its time derivative, $H_\tau(\xi,\eta,\zeta)$. A schematic for computational grid is shown in Fig. 2 for two-dimensional grids.

In the shock-fitting method, the unsteady shock is treated as a boundary of the computational domain governed by

$$\eta(x,y,z,t) = \eta_{\max} = \text{constant} \tag{12}$$

The interaction between the shock and disturbances is solved as a part of solutions. The position and velocity of the shock front, represented by $H(\xi,\eta,\zeta)$ and $H_\tau(\xi,\eta,\zeta)$, are taken as independent flow variables that are solved by high-order finite-difference methods.

Different types of shock-fitting methods can be constructed based on the choice of two main aspects:

(a) Algorithms to compute shock movements.
(b) Methods to approximate the spatial derivatives in flow field Eq. (10).

In this paper, we evaluate numerical accuracy of seven shock-fitting schemes based on different methods of computing shock velocities and different algorithms for discretizing the spatial derivatives in the flow equations. Table 1 shows the naming convention adopted in this paper for the identification of different shock-fitting methods. There are two parts in the name of a shock-fitting method: the first part represents the shock-advancing method, and the second represents the algorithm for spatial derivatives in flow equations. Therefore, Methods A-u, B-u and C-u use different methods, A, B and C, respectively, of shock-velocity calculations, while they all use the same 5th-order upwind scheme for spatial derivatives. We also consider shock-fitting methods using four different methods of implementation of the WENO schemes for spatial derivatives, which can be coupled with one of the three shock-advancing methods A, B or C. The first of these methods is termed Method A-w1 in Table 1, which represents the use of the first WENO method coupled with Method A for the shock-advancing method. To evaluate the effects of spatial algorithms, we only consider Methods A-w1 to A-w4 in this paper.

3.1. Various algorithms to determine shock velocity

One of the most important aspects of a shock-fitting method is to correctly predict the shock velocity within the shock-fitting code. Shock velocity is needed to find the position of the shock-front, which governs the boundary of the computational domain. Moreover, shock velocity coupled with Rankine–Hugoniot conditions determines the flow variables just behind the shock. Hence, accuracy of shock velocity is expected to have a significant effect on the overall accuracy of the shock-fitting scheme. The three such methods used in the currently study, listed in Table 1, are described in this section.

This paper considers only inviscid problems. However, even for solving the Navier Stokes equations, it is a general practice to use shock fitting implementations with Rankine Hugoniot jump conditions assuming the shock waves to be infinitely thin and governed by the Euler equations (only at the shock). This is valid when the thickness of the shock wave is very small as compared to the smallest length scales in the flow. For example, smallest length scale in turbulent flows is Kolmogorov scale which is one to two orders larger than shock thickness in sufficiently high-speed flows [36,70]. Hence, shock-fitting algorithms with assumption of infinitely thin shocks are expected to closely mimic the physics even with the viscous flows. Such implementation of shock-fitting algorithm has been widely used in past for solving Navier Stokes equations where

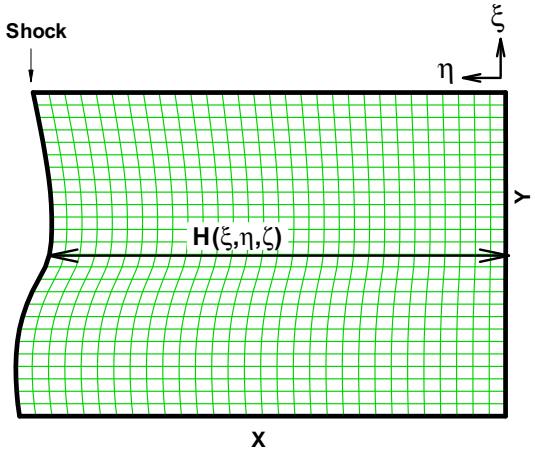

Fig. 2. Schematic of 2-D shock-fitting grids shown for shock-disturbance interactions.

Table 1
Naming convention of the seven moving-grid shock-fitting methods considered in this paper.

Name	(a) Method for computing shock velocities		(b) Method for discretizing flow-field equations	
	Method	Section	Method	Section
Method A-u	Time derivative of R–H relations with a characteristic relation [58]	3.1.1	5th order upwind [58]	3.2.1
Method B-u	Time derivative of R–H relations with a momentum equation	3.1.2	Same as Method A-u	3.2.1
Method C-u	Shock velocity directly computed by Riemann invariants	3.1.3	Same as Method A-u	3.2.1
Method A-w1	Same as Method A-u	3.1.1	5th order WENO5 [69] with Eq. (49) for local approximation at shock	3.2.2
Method A-w2	Same as Method A-u	3.1.1	5th order WENO5 [69] with Eq. (50) for local approximation at shock	3.2.2
Method A-w3	Same as Method A-u	3.1.1	5th order WENO5M [68] Eq. (49) for local approximation at shock	3.2.2
Method A-w4	Same as Method A-u	3.1.1	5th order WENO5M [68] with Eq. (50) for local approximation at shock	3.2.2

accuracy of the solutions is critical for reliable simulations. Examples include stability and receptivity of hypersonic boundary layers [62], flows over blunt bodies [56], and shock–turbulence interactions [36].

3.1.1. Method A: time derivative of R–H relations with a characteristic relation

In this method, the velocity of the shock front is determined from a shock acceleration relation as described in detail by Zhong [58]. This relation is obtained by taking a derivative of the Rankine–Hugoniot relations across the main shock and using a characteristic compatibility relation from behind the shock. The location of the shock is obtained from shock-velocity relations and the grid is modified to follow motions of the shock.

The Rankine–Hugoniot conditions relate the flow variables across the shock, which can be written in terms of flux vectors as:

$$\mathbf{F}'_s = \mathbf{F}'_0 \tag{13}$$

where $\mathbf{F}'_s$ is the flux vector immediately behind the shock along the η grid line (Fig. 2) in the computational domain and $\mathbf{F}'_0$ represents the flux vector along the η grid line on the free-stream side of the shock front. The above equation leads to the jump conditions across the shock

$$\begin{aligned}
p_s &= p_0\left[1+\frac{2\gamma}{\gamma+1}\left(M_{n0}^2-1\right)\right]\\
\rho_s &= \rho_0\left[\frac{(\gamma+1)M_{n0}^2}{(\gamma-1)M_{n0}^2+2}\right]\\
u_{ns} &= v_n+\frac{\rho_0}{\rho_s}(u_{n0}-v_n)\\
\vec{\mathbf{u}}_{ts} &= \vec{\mathbf{u}}_{t0}=\vec{\mathbf{u}}_0-u_{n0}\vec{\mathbf{n}}\\
\vec{\mathbf{u}}_s &= \vec{\mathbf{u}}_{ts}+u_{ns}\vec{\mathbf{n}}
\end{aligned} \tag{14}$$

where $\vec{\mathbf{n}}$ is the local normal vector of the shock front and v_n is the velocity of shock motion $\vec{\mathbf{n}}$ direction which are related to grid transformation metrics for Eq. (9) as:

$$\vec{\mathbf{n}} = \frac{\eta_x\hat{i}+\eta_y\hat{j}+\eta_z\hat{k}}{|\nabla\eta|} \quad \text{where } |\nabla\eta| = \sqrt{\eta_x^2+\eta_y^2+\eta_z^2} \tag{15}$$

$$v_n = -\frac{\eta_t}{|\nabla\eta|} \tag{16}$$

Here the subscripts "s" and "0" represent flow variables behind the shock and on the free-stream side of the shock, respectively. M_{n0} is the normal component of free-stream Mach Number relative to the shock front. $\vec{\mathbf{u}}$ and $\vec{\mathbf{u}}_t$ are velocity vector and tangential velocity vector, respectively while u_n is the component of velocity along $\vec{\mathbf{n}}$ direction.

If the velocity of the shock front, v_n, is computed, the flow variables behind the shock can be calculated using the jump conditions (Eq. (14)). A characteristic compatibility relation from behind the shock is used to determine the shock normal velocity v_n. From the governing Eq. (10) we have:

$$\frac{1}{J}\frac{\partial\mathbf{U}}{\partial\tau}+\frac{\partial\mathbf{F}'}{\partial\eta} = -\frac{\partial\mathbf{E}'}{\partial\xi}-\frac{\partial\mathbf{G}'}{\partial\zeta}-\mathbf{U}\frac{\partial(1/J)}{\partial\tau} \tag{17}$$

This equation is evaluated at the point immediately behind the shock. In the equations, the Jacobian matrix $B'_s = \partial F'_s/\partial U$, has the eigenvalues

$$\frac{|\nabla\eta|}{J}(u_n - v_n)_s, \ldots, \frac{|\nabla\eta|}{J}(u_n - v_n)_s, \frac{|\nabla\eta|}{J}(u_n - v_n - c)_s, \frac{|\nabla\eta|}{J}(u_n - v_n + c)_s \tag{18}$$

where c is speed of the sound. The corresponding left eigenvectors are $\mathbf{I}_1, \mathbf{I}_2, \ldots, \mathbf{I}_{N-1}, \mathbf{I}_N$, where N is the number of independent variables in the equations, and

$$\mathbf{I}_N = \frac{1}{2c^2}\begin{bmatrix} (\gamma-1)(u^2+v^2+w^2) - 2cu_n \\ cn_x - (\gamma-1)u \\ cn_x - (\gamma-1)v \\ cn_x - (\gamma-1)w \\ \gamma - 1 \end{bmatrix} \tag{19}$$

The left eigenvector behind the shock satisfies

$$\mathbf{I}_N \cdot B'_s = \frac{|\nabla\eta|}{J}(u_n - v_n + c)_s \mathbf{I}_N \tag{20}$$

The characteristic field approaching the shock from behind corresponds to the eigenvalue $(\nabla\eta/J)(u_n - v_n + c)_s$. The corresponding eigenvector is $\mathbf{I}_N$. The compatibility relation at a grid point immediately behind the shock for this characteristic field can be obtained by multiplying Eq. (17) by $\mathbf{I}_N$,

$$\mathbf{I}_N \cdot \left(\frac{\partial \mathbf{U}}{\partial\tau}\right) = \mathbf{I}_N \cdot \left(-\frac{\partial \mathbf{E}'}{\partial\xi} - \frac{\partial \mathbf{F}'}{\partial\eta} - \frac{\partial \mathbf{G}'}{\partial\zeta} - \frac{\partial \mathbf{E}'_v}{\partial\xi} - \frac{\partial \mathbf{F}'_v}{\partial\eta} - \frac{\partial \mathbf{G}'_v}{\partial\zeta} - \mathbf{U}\frac{\partial(1/J)}{\partial\tau}\right)J \tag{21}$$

On the other hand shock jump condition (13) can be rewritten as

$$[F'] = (\mathbf{F}_s - \mathbf{F}_0)\cdot\mathbf{a} + [U_s - U_0]b = 0 \tag{22}$$

where

$$\begin{aligned} \mathbf{a} &= (\eta_x/J)_s\mathbf{i} + (\eta_y/J)_s\mathbf{j} + (\eta_z/J)_s\mathbf{k} \\ b &= (\eta_t/J)_s \end{aligned} \tag{23}$$

Taking derivative of Eq. (22) with respect to τ in the computational space leads to

$$B'_s\partial U_s/\partial\tau - B'_0\partial U_0/\partial\tau + (\mathbf{F}_s - \mathbf{F}_0)\cdot\partial\mathbf{a}/\partial t + (U_s - U_0)\partial b/\partial\tau = 0 \tag{24}$$

where the flux Jacobian $B' = \partial F'/\partial U$, is the Jacobian of the η direction flux defined in the conservation Eqs. (10) and

$$\begin{aligned} \frac{\partial\mathbf{a}}{\partial\tau} &= \frac{\partial(\eta_x/J)_s}{\partial\tau}\mathbf{i} + \frac{\partial(\eta_y/J)_s}{\partial\tau}\mathbf{j} + \frac{\partial(\eta_z/J)_s}{\partial\tau}\mathbf{k} \\ \frac{\partial b}{\partial\tau} &= \frac{\partial(\eta_t/J)_s}{\partial\tau} \end{aligned} \tag{25}$$

These time derivatives of the grid metrics can be derived by the same methods as those used in the discretization of the interior equations.

The equation for shock velocity can now be obtained by multiplying both sides of Eq. (24) by $\mathbf{I}_N$ and using Eq. (20), i.e.

$$\frac{\partial b}{\partial\tau} = \frac{-1}{[\mathbf{I}_N\cdot(U_s - U_0)]}\left[\frac{|\nabla\eta|}{J}(u_n - v_n + c)_s\mathbf{I}_N\cdot\left(\frac{\partial U}{\partial\tau}\right)_s + \mathbf{I}_N\cdot(\mathbf{F}_s - \mathbf{F}_0)\cdot\frac{\partial\mathbf{a}}{\partial t} - (\mathbf{I}_N.B'_0)\frac{\partial U_0}{\partial\tau}\right] \tag{26}$$

where the term $\mathbf{I}_N\cdot(\partial U/\partial\tau)_s$ is computed using the characteristic relation (21), in which the spatial derivatives are discretized using one-sided finite-difference scheme together with the discretization of the interior points for the Eq. (10). In the Eq. (26) $\partial b/\partial\tau$ and $\partial\mathbf{a}/\partial\tau$ can be expressed as a function of H and H_τ as

$$\frac{\partial b}{\partial\tau} = d_1(\xi,\zeta,H,H_\tau) + d_2(\xi,\zeta,H,H_\tau)\frac{\partial H_\tau}{\partial\tau} \tag{27}$$

$$\frac{\partial\mathbf{a}}{\partial\tau} = \mathbf{g}(\xi,\zeta,H,H_\tau) \tag{28}$$

where $H = H((\xi,\zeta,\tau)$ is the distance between the shock and the wall along η = constant grid line (as shown in Fig. 2), and $H_\tau = \partial H/\partial\tau$. The coefficients d_1, d_2 and vector $\mathbf{g}$ are functions of grid metrics.

Eqs. (26)–(28) yield governing equations for the shock motions for two independent variables, $H$and H_τ, in the form

$$\begin{aligned}\frac{\partial H_\tau}{\partial \tau} &= f\left(\xi, \zeta, \mathbf{U_s}, \mathbf{I}_N \cdot \left(\frac{\partial \mathbf{U}_s}{\partial \tau}\right), \mathbf{U}_0, \left(\frac{\partial \mathbf{U}_0}{\partial \tau}\right), H, H_\tau\right) \\ \frac{\partial H}{\partial \tau} &= H_\tau\end{aligned} \tag{29}$$

The equations specified in Eq. (29) along with Eq. (10) form a system of equations in flow variables, shock position, and shock velocity. The resulting equations are solved using explicit Runge–Kutta schemes.

3.1.2. Method B: time derivative of R–H relation together with a momentum equation

Henrick et al. [68] use a different method to find the shock acceleration using the momentum equation along the shock normal direction instead of a characteristic relation. Conservation of mass across the shock wave gives

$$\rho_s u_{ns} = \rho_s v_n + \rho_0 (u_{n0} - v_n) \tag{30}$$

Using $\rho_s = \rho_0\left[(\gamma+1)M_{n0}^2/\{(\gamma-1)M_{n0}^2+2\}\right]$ (from Eq. (14)) and $M_{n0}^2 = \rho_0 u_{n0}^2/\gamma p_0$ leads to the momentum in the normal direction as follows:

$$\rho_s u_{ns} = \frac{\rho_0(v_n - u_{n0})\{\gamma(\rho_0(v_n - u_{n0})u_{n0} - 2p_0) + \rho_0(2v_n^2 - 3v_n u_{n0} + u_{n0}^2)\}}{\gamma(2p_0 + \rho_0(v_n - u_{n0})^2) - \rho_0(v_n - u_{n0})^2}, \tag{31}$$

where, u_n is the flow velocity normal to the shock and v_n is the velocity of the shock. Henrick et al. [68] use this relation to find the shock acceleration in one-dimensional detonation problems. Noting that momentum $\rho_s u_{ns}$ in Eq. (31) is only function of shock velocity, shock acceleration can be written as chain rule as follows for a one-dimensional problem.

$$\frac{dv_n}{d\tau} = \left(\frac{d(\rho_s u_{ns})}{dv_n}\right)^{-1} \cdot \left(\frac{d(\rho_s u_{ns})}{d\tau}\right) \tag{32}$$

One can take the derivative of Eq. (31) with respect to shock velocity to obtain $d(\rho_s u_{ns})/dv_n$ while the term $(d(\rho_s u_{ns})/d\tau)$ is computed directly as one solves the momentum Eq. (2). The method described here is similar to, but more general than, the shock-fitting method of Henrick et al. [68], where they solve one-dimensional governing equations in a reference frame fixed to the shock front.

3.1.3. Method C: shock velocity directly computed by Riemann invariants

An alternative to shock acceleration based methods is to compute the shock velocity directly using the value of a Riemann invariant from behind the shock. This method is simple to implement, and most early shock-fitting methods used this idea to compute shock velocity [37,43]. Only a one-dimensional example is described here. The method can be easily extended to multi-dimensional problems.

For an unsteady one-dimensional flow, a schematic of the shock and trajectories of C_+ characteristics emanating from the grid points behind the shock is shown in Fig. 3. The flow on the right of the shock is approaching the shock with supersonic speed relative to the shock, and flow behind (left of) the shock is subsonic in the shock reference frame. Flow variables ahead of the shock are known while shock-fitting methodology is used to compute the flow behind the shock. To compute the shock velocity consistent to the physics for this configuration, the method should use one characteristic (C_+) wave coming from behind the shock along with the information from the supersonic region ahead of the shock. Along the C_+ line behind the shock, defined by $dx/dt = u + c$, we have a constant Riemann invariant given by

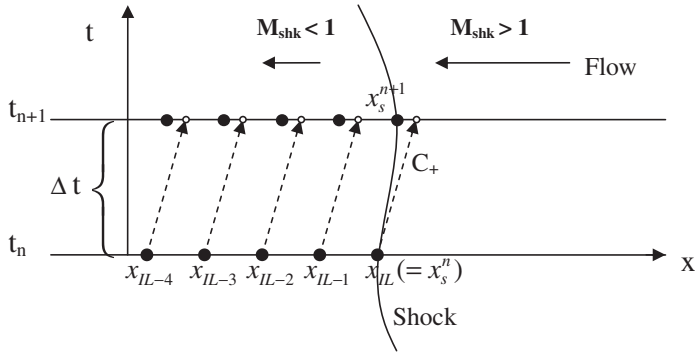

Fig. 3. Finding shock velocity based on value of Riemann invariant from behind the shock (J_s^+).

$$J_s^+ = u_s + 2c_s/(\gamma_s - 1) \tag{33}$$

Using $c_s = c_0(p_s/p_0)^{1/2}(\rho_0/\rho_s)^{1/2}$ and Rankine Hugoniot relations for u_s, p_s and ρ_s from Eqs. (14) and (33) leads to following relation between J_s^+ and flow variables in front of the shock:

$$\frac{J_s^+}{c_0} = \frac{2(M_1^2-1)}{(\gamma_s+1)M_1} + \frac{u_0}{c_0} + \frac{2}{(\gamma_s-1)}\sqrt{\left[1+\frac{2\gamma_s(M_1^2-1)}{(\gamma_s+1)}\right]\left[\frac{2+(\gamma_s-1)M_1^2}{(\gamma_s+1)M_1^2}\right]} \tag{34}$$
$$M_1 = (v_s - u_0)/c_0$$

where c_0 is the speed of sound upstream of the shock and v_s is velocity of the shock. The Mach number of the supersonic flow relative to shock is denoted by M_1. Once the J_s^+ value is known behind the shock, the shock velocity can be found using a numerical method to solve Eq. (34). With known values of flow-field variables, shock velocity v_s^n and shock location x_s^n at a time t_n (Fig. 3), one can find the velocity v_s^{n+1}at new time step, $t_{n+1} = t_n + \Delta t$, using the following algorithm:

1. Advance the shock to new position, $x_s^{n+1} = x_s^n + \Delta t \cdot v_s^n$.
2. Choose an appropriate number of grid points (5 in current study) behind the shock at time t_n, and find the location of C_+ lines ($dx/dt = u + c$) originating from these points at time t_{n+1}. The values of Riemann invariant $J^+ = u + 2c/(\gamma - 1)$ at the chosen grid points are also computed and stored.
3. Using locations of C_+ lines originating from chosen grid points and corresponding J^+ values found in step 2, interpolate to obtain the Riemann invariant behind the shock J_s^+ corresponding to x_s^{n+1} location at t_{n+1}.
4. With the known value of J_s^+, solve Eq. (34) to obtain v_s^{n+1}.

The shock velocity is thus obtained at the new time without needing to find the shock acceleration values.

3.2. Methods for discretizing flow-field equations

Shock-fitting methodology can be applied with any scheme for approximating spatial derivatives in the computational domain away from the shock. In the current study we use a 5th order upwind scheme as well as 5th order WENO schemes (Table 1) which are described next.

3.2.1. Fifth order upwind finite-difference scheme (used in Method A-u)

In this method, an explicit finite-difference scheme from Ref. [58] is used for spatial discretization of the governing Eq. (10). The flux terms are discretized by a fifth-order upwind scheme. For the inviscid flux vectors, the flux Jacobians contain both positive and negative eigenvalues. A local Lax–Friedrichs scheme is used to split vectors into negative and positive wave fields. For example, the flux term F' in Eq. (10) can be split into two terms of positive and negative eigenvalues as follows:

$$F' = F'_+ + F'_- \tag{35}$$

where $F'_+ = (F' + \lambda U)/2$ and $F'_- = (F' - \lambda U)/2$ and λ is chosen to be larger than the local maximum eigenvalue of F', i.e.,

$$\lambda = \frac{|\nabla\eta|}{J}\left(\sqrt{(\varepsilon c)^2 + u'^2} + c\right) \tag{36}$$

where

$$u' = \frac{\eta_x u + \eta_y v + \eta_z w + \eta_t}{|\nabla\eta|} \tag{37}$$

The parameter ε is a small positive dimensionless constant added to adjust the smoothness of the splitting. The fluxes F'_+ and F'_- contain only positive and negative eigenvalues, respectively. Therefore, in the spatial discretization of Eq. (10), the derivative of the flux F' is split into two terms

$$\frac{\partial F'}{\partial \eta} = \frac{\partial F'_+}{\partial \eta} + \frac{\partial F'_-}{\partial \eta} \tag{38}$$

where the first term on the right hand side is discretized by the upwind scheme and the second term by the downwind scheme. Other terms in Eq. (10) are treated similarly.

The fifth-order explicit scheme utilizes a 7-point stencil and has an adjustable parameter α as follows:

$$u'_i = \frac{1}{hb_i}\sum_{k=-3}^{3} a_{i+k}u_{i+k} - \frac{\alpha}{6!b_i}h^5\left(\frac{\partial^6 u}{\partial x^6}\right)_i + \cdots \tag{39}$$

where $a_{i\pm3} = \pm1 + \alpha/12$, $a_{i\pm2} = \mp9 - \alpha/2$, $a_{i\pm1} = \pm45 + 5\alpha/4$, $a_i = -5\alpha/3$ and $b_i = 60$. The scheme is upwind when $\alpha < 0$ and downwind when $\alpha > 0$. It becomes a 6-order central scheme when $\alpha = 0$. For a 5th order upwind scheme, a typical value of $\alpha = -6.0$ is used.

3.2.2. Fifth order WENO schemes: WENO5 and WENO5M

In the typical shock–turbulence interaction problem (Fig. 1), the flow behind the main shock may encounter formation of weak secondary shocks. Hence, even as the main shock is fitted, a shock-capturing scheme may be needed to compute the flow behind the fitted main shock. We have combined the shock-fitting algorithm with two 5th order WENO schemes. The first WENO scheme is based on Jiang and Shu's [69] formulations, which will be referred in this paper as the WENO5 scheme. Henrick et al. [68] suggested an improvement over the WENO5 scheme to obtain more accurate solutions in the smooth region. This scheme is referred in this study as the WENO5M scheme.

In the WENO5 scheme, a spatial derivative of any scalar function f is approximated as follows:

$$\left.\frac{\partial f(u)}{\partial x}\right|_{x=x_j} \approx \frac{\hat{f}_{j+1/2}-\hat{f}_{j-1/2}}{\Delta x} \tag{40}$$

where $\hat{f}_{j+1/2}$ is an approximation to the numerical flux function which is constructed from a weighted sum of fluxes from three different three point stencils as:

$$\hat{f}_{j+1/2} = \omega_1\hat{f}^{(1)}_{j+1/2} + \omega_2\hat{f}^{(2)}_{j+1/2} + \omega_3\hat{f}^{(3)}_{j+1/2} \tag{41}$$

where,

$$\begin{aligned}
\hat{f}^{(1)}_{j+1/2} &= \frac{1}{3}f_{j-2} - \frac{7}{6}f_{j-1} + \frac{11}{6}f_j \\
\hat{f}^{(2)}_{j+1/2} &= -\frac{1}{6}f_{j-1} + \frac{5}{6}f_j + \frac{1}{3}f_{j+1} \\
\hat{f}^{(3)}_{j+1/2} &= \frac{1}{3}f_j + \frac{5}{6}f_{j+1} - \frac{1}{6}f_{j+2}
\end{aligned} \tag{42}$$

and ω_i are nonlinear weights given by

$$\omega_i = \frac{\sigma_i}{\sum_{k=1}^{3}\sigma_k}, \quad \text{where} \quad \sigma_i = \frac{\gamma_i}{(\varepsilon^* + \beta_k)^2} \tag{43}$$

Here, γ_i represent the ideal weights, which correspond to 5th order scheme with Eq. (23) and are given as

$$\gamma_1 = \frac{1}{10}, \quad \gamma_2 = \frac{3}{5}, \quad \gamma_3 = \frac{3}{10} \tag{44}$$

and the indicators of smoothness, β_k, are given by:

$$\begin{aligned}
\beta_1 &= \frac{13}{12}(f_{j-2} - 2f_{j-1} + f_j)^2 + \frac{1}{4}(f_{j-2} - 4f_{j-1} + 3f_j)^2 \\
\beta_2 &= \frac{13}{12}(f_{j-1} - 2f_j + f_{j+1})^2 + \frac{1}{4}(f_{j-1} - f_{j+1})^2 \\
\beta_3 &= \frac{13}{12}(f_j - 2f_{j+1} + f_{j+2})^2 + \frac{1}{4}(3f_j - 4f_{j+1} + f_{j+2})^2
\end{aligned} \tag{45}$$

The parameter ε^* is a constant used to keep the weights bounded. Eqs. (40)–(45) describe the WENO5 scheme and, generally, $\varepsilon^* = 10^{-6}$ is used to obtain a fifth order accuracy in the smooth region while keeping the solution stable near discontinuities.

In the WENO5M scheme, Henrick et al. [68] suggest that solution accuracy can be improved by mapping the weights in Eq. (43) to get the final weights as

$$\bar{\omega}_i = \frac{g_i(\omega_i)}{\sum_{k=1}^{3} g_k(\omega_k)} \tag{46}$$

where $g_k(\omega)$ is the mapping function given by

$$g_k(\omega) = \frac{\omega(\sigma_{k+}\sigma_k^2 - 3\sigma_k\omega + \omega^2)}{\sigma_k^2 + (1-2\sigma_k)\omega} \tag{47}$$

Instead of Eq. (41), the WENO5M scheme uses following equation with $\varepsilon^* = 10^{-40}$:

$$\hat{f}_{j+1/2} = \bar{\omega}_1\hat{f}^{(1)}_{j+1/2} + \bar{\omega}_2\hat{f}^{(2)}_{j+1/2} + \bar{\omega}_3\hat{f}^{(3)}_{j+1/2} \tag{48}$$

As detailed in [68,69], for the Euler equations, a simple local Lax–Friedrichs flux splitting is first carried out for flux terms in all directions following Eqs. (35)–(38) to divide the flux vectors into negative and positive wave fields. The procedure for finding smoothness indicators β_k and weights ω_i (for the WENO5 scheme) or $\bar{\omega}_i$ (for the WENO5M schemes) is carried out in local characteristic fields. We find a Roe average [71] of grid point values and then, based on eigenvectors of Jacobian, transform all the quantities needed for evaluating numerical fluxes to local characteristic fields. The numerical fluxes in each

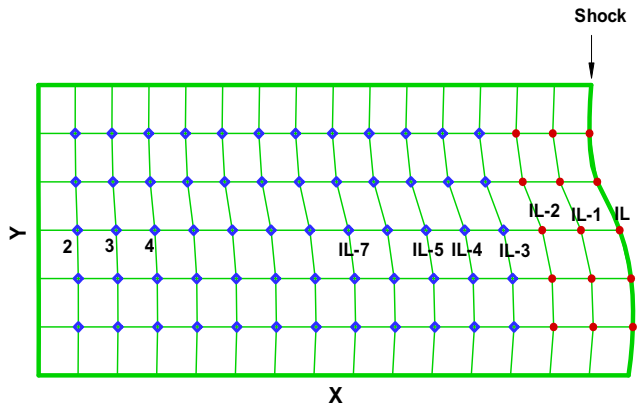

Fig. 4. For application of shock-fitting with 5th order WENO schemes, upwind finite differencing is used for points close to shock (shown by filled circles) while WENO scheme is applied for the interior (shown by hollow circles).

characteristic field are found by using the scalar procedure described above (Eqs. (41)–(48)), followed by a transformation back to original physical space.

In general, weights are modified in WENO schemes such that essentially one-sided stencils are used near the boundary points. Shock is treated like a boundary in the shock-fitting method. In fact, our standard shock-fitting Method A-u [58] needs flux values at the shock points to find the shock acceleration, which is then used to calculate the advancement of the shock. Since the fifth-order WENO schemes described above need three grid points on either side to compute fluxes at any point, we use one-sided finite-difference scheme for the grid points near the shock. In this way, the WENO stencil does not cross the shock. We choose to use fix stencil for the points near the shock boundary so as to better control the accuracy. Such one-sided stencils have been used successfully by other researchers with shock-fitting [68]. Fig. 4 shows a schematic of the computational domain highlighting the points where one-sided difference should be used. Specifically, if the shock lies on the grid line represented as $I = IL$, one-sided finite differencing is used for points with $I = IL-2, IL-1, IL$. There are many choices available for one-sided finite-difference schemes for the three grid points close to the shock boundary. In this study we consider both the WENO5 and WENO5M schemes along with following one-sided 5-point finite-difference formulas near the shock.

$$\begin{aligned}
\left.\frac{\partial f}{\partial x}\right|_{I=IL} &\approx \frac{1}{12\Delta x}(3f_{IL-4} - 16f_{IL-3} + 36f_{IL-2} - 48f_{IL-1} + 25f_{IL}) + O(\Delta x^4)\\
\left.\frac{\partial f}{\partial x}\right|_{I=IL-1} &\approx \frac{1}{12\Delta x}(-f_{IL-4} + 6f_{IL-3} - 18f_{IL-2} + 10f_{IL-1} + 3f_{IL}) + O(\Delta x^4)\\
\left.\frac{\partial f}{\partial x}\right|_{I=IL-2} &\approx \frac{1}{12\Delta x}(f_{IL-4} - 8f_{IL-3} + 8f_{IL-1} - f_{IL}) + O(\Delta x^4)
\end{aligned} \tag{49}$$

The one-sided formulas in Eq. (49) are 4th order accurate. Henrick et al. [68] suggest using following combination of one-sided approximation near the shock, which have also been considered to use with WENO5 and WENO5M in this study.

$$\begin{aligned}
\left.\frac{\partial f}{\partial x}\right|_{I=IL} &\approx \frac{1}{60\Delta x}(-12f_{IL-5} + 75f_{IL-4} - 200f_{IL-3} + 300f_{IL-2} - 300f_{IL-1} + 137f_{IL}) + O(\Delta x^5)\\
\left.\frac{\partial f}{\partial x}\right|_{I=IL-1} &\approx \frac{1}{12\Delta x}(-f_{IL-4} + 6f_{IL-3} - 18f_{IL-2} + 10f_{IL-1} + 3f_{IL}) + O(\Delta x^4)\\
\left.\frac{\partial f}{\partial x}\right|_{I=IL-2} &\approx \frac{1}{60\Delta x}(-2f_{IL-5} + 15f_{IL-4} - 60f_{IL-3} + 20f_{IL-2} - 30f_{IL-1} - 3f_{IL}) + O(\Delta x^5)
\end{aligned} \tag{50}$$

Combinations of the WENO5 and WENO5M schemes with application of Eqs. (49) and (50) near the shock give rise to four different ways of discretizing flow-field equations in a shock-fitting method. Shock-fitting methods coupling these four different WENO schemes with method A of finding shock-velocity have been considered in this paper and are referred in Table 1 as Methods A-w1 to A-w4.

4. A new front-tracking based high-order shock-fitting method

The conventional moving-grid shock-fitting methodology assumes the shock to be the boundary of the domain and flow is solved on moving grids. However, this approach becomes difficult to apply for a problem where shock geometry becomes complex or the shock performs large motions. Hence, it is useful to develop a methodology that can implement ideas of a

shock-fitting algorithm on fixed grids. In this section, we present and evaluate a new fixed grid shock-fitting method, where the shock is treated as an interface that can move across fixed grid points. Such idea was explored in past as floating shock-fitting methods by Moretti [49]. The method is similar to fixed grid Cartesian grid methods, such as the Immersed Boundary Method (IBM) [72], Immersed Interface Method (IIM) [73], and Ghost-fluid method [74] coupled with methods to track the front [75–77].

4.1. Shock front definition and geometric parameters

In our methodology, the shock-front is assumed to be sharp and is represented using Lagrangian marker points. The shock front is represented by the marker points through 4th order piecewise polynomial interpolations. For convenience in taking one-sided finite differences at the shock front, intersection points of the front with the grid lines are chosen as marker points. Fig. 5 shows typical marker points (S_i,S_{i+1}, etc.) for a shock-front moving across a two-dimensional grid. These marker points are stored in a sequenced list. The order in the list indicates the immediate neighboring markers of a marker as shown in the Fig. 5.

The notation used here is such that as we move along the markers by incrementing in this sequenced list, the low-pressure side of the shock should be on the left. With each marker point, information regarding geometry of the front, flow properties corresponding to the marker points and relation of marker point with the fixed grid is also needed to be saved.

Coordinates of the marker points are computed and saved for each marker points. A critical part of information regarding shock-geometry for the shock-fitting method is shock shape, specifically, the shock normal and tangential unit vectors which are obtained using the coordinates. We use the following parametric representation for the marker points to obtain shock normal and shock tangential unit vectors:

$$\begin{aligned} x &= x(s) \\ y &= y(s) \end{aligned} \tag{51}$$

where s represents the arclength along the interface. Arclength is chosen as the parameter to represent the surface since arclength value monotonically increases along the surface and each value of arclength coordinate correspond to a unique point on the interface. Moreover, s represents the value of the local coordinate in the tangential direction which can be readily used to obtain tangential derivatives of various flow variables where needed. Using s as a parameter, we define components of the normal and tangential unit vectors in 2-D as follows:

$$\begin{aligned} n_x &= \frac{\partial y/\partial s}{\left[(\partial x/\partial s)^2 + (\partial y/\partial s)^2\right]^{\frac{1}{2}}}, \quad n_y = \frac{-\partial x/\partial s}{\left[(\partial x/\partial s)^2 + (\partial y/\partial s)^2\right]^{\frac{1}{2}}}, \\ \tau_{1x} &= \frac{\partial x/\partial s}{\left[(\partial x/\partial s)^2 + (\partial y/\partial s)^2\right]^{\frac{1}{2}}}, \quad \tau_{1y} = \frac{\partial y/\partial s}{\left[(\partial x/\partial s)^2 + (\partial y/\partial s)^2\right]^{\frac{1}{2}}}. \end{aligned} \tag{52}$$

This way of computing local unit vectors ensures that the normal vector points from the high-pressure side towards the low-pressure side (Fig. 5). Thus, using the direction of the normal vector at any marker point, we are able to identify the high and low-pressure sides of the shock with respect to the given marker point.

It is noted, however, that it is not trivial to find high-order approximations to arclength using the coordinates of the marker points. For a curve represented by a set of marker points with coordinates (x_j, y_j), $j = 1,2,\ldots,N$, following iterative procedure is used to find the arclength s consistent with polynomial interpolations:

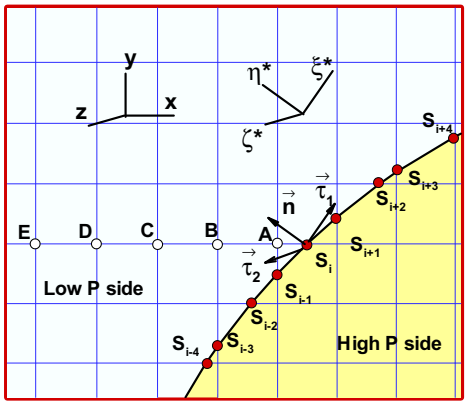

Fig. 5. Schematic for arrangement of marker points and stencil for one-sided differentiation for the fixed-grid-shock-fitting methodology. A local natural coordinate system (ξ^*, η^*, ζ^*) used for computation of shock front velocity at marker point S_i is also shown.

0. Initialize an approximate value of arclength, t_k, as a summed distance between the marker points:

$$t_k = \sum_{j=2}^{k} \sqrt{(x_j - x_{j-1})^2 + (y_j - y_{j-1})^2} \quad (k = 2, 3, \ldots, N), \tag{53}$$

1. From $x_k = x_k(t_k)$ and $y_k = y_k(t_k)$, find 5th order polynomials $x = x(t)$, $y = y(t)$ through each marker point,
2. Carry out numerical integration to update the value of approximate arclength at each point as follows:

$$t_k^* = \sum_{i=1}^{k} \int_{t_i}^{t_{i+1}} \sqrt{\left[(dx/dt)^2 + (dy/dt)^2\right]^{\frac{1}{2}}} dt, \tag{54}$$

3. If $|t_k^* - t_k| \geqslant \varepsilon_s$ (an error tolerance value), go to Step 1 with $t_k = t_k^*$; otherwise exit the loop with $s_k = t_k^*$.

In our tests it was found that generally less than five such iterations were required for an error tolerance value of $\varepsilon_s = 10^{-10}\Delta x$.

4.2. Finite difference schemes for irregular grid points near shock front

In the present fixed-grid shock-fitting scheme, we use the same algorithms as those of the conventional shock-fitting Method A-u for regular grid points away from the shock. Thus, Eqs. (1)–(11) are still applicable in this formulation, except fixed grids are used with a constant Jacobian of grid transformation. The 5th order upwind method given by Eq. (39) can be used on the regular points where finite-difference stencil does not cross the shock front. However, special treatment is needed for the "irregular" points where the stencil requires points on both sides of the shock. For example in Fig. 5, grid points 'D' and 'E' are regular grid points because a seven point stencil needed for the fifth-order upwind scheme at these points does not cross the shock. On the other hand, grid points 'A', 'B' and 'C' are irregular points in this example. There are irregular grid points on both sides of the shock along x, as well as y-direction grid lines.

The flow ahead (low-pressure side) of the shock is supersonic with respect to the shock and does not need any information from the shock. Information from the low-pressure side of the shock is duly taken into account based on the direction of flow characteristics and Rankine Hugoniot jump conditions. Thus, separate stencils can be used on either side of the shock in the front-tracking based shock-fitting scheme. To avoid crossing the discontinuous shock-front by the grid stencils, we use one-sided finite differencing on the irregular points. For calculation of the first x derivative of a variable u with $n-1$th order of accuracy, we use a polynomial interpolation based on a set of n points, $\mathbf{I}_n$, which is represented by x coordinate values: $x_1, x_2, \ldots, x_n$. The derivative of any variable u at a point x_j (where $j \in \mathbf{I}_n$) is given as follows:

$$\left[\frac{\partial u}{\partial x}\right]_{x=x_j} = \sum_{i \in \mathbf{I}_n} l_i^{n'}(x_j) u(x_i) \tag{55}$$

where $l_i^n(x)$ is the ith Lagrange basis polynomial on $\mathbf{I}_n$ given by

$$l_i^n(x) = \prod_{k \in \mathbf{I}_n,\, \neq i} (x - x_k) \Big/ \prod_{k \in \mathbf{I}_n,\, \neq i} (x_i - x_k) \tag{56}$$

We use 4th order accurate derivatives at the irregular grid points and 5th order upwind scheme of Zhong [58] at regular points. Fig. 6 shows an example of the points used in the stencil for finding the first x derivatives of flow variables at irregular points (P_{i-2}, P_{i-1} and P_i) in the low-pressure side of the shock. Along with the interface point (P_Γ), the one-sided stencil consists of grid points in the low-pressure side along a horizontal grid line (points P_i, P_{i-1}, etc.). When one-sided derivatives are computed, there might be issues with method stability if the stencil has one of the grid points too close to the interface. In this case, that grid point should be removed from the interpolation stencil in order to maintain numerical stability. Hence the choice of stencil is based on the separation of interface point P_Γ from the nearest grid point P_i represented by

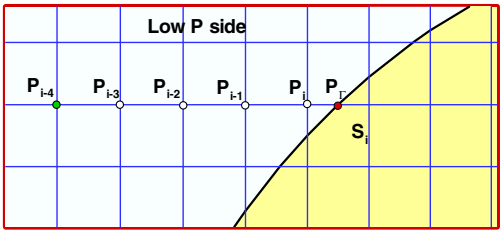

Fig. 6. Stencil used for 4th order approximation of first x derivatives of flow variables at irregular grid points. If $\sigma \geqslant \sigma^*$ the stencil consists of points P_{i-3}, P_{i-2}, P_{i-1}, P_i and P_Γ. If $\sigma < \sigma^*$ points P_{i-4}, P_{i-3}, P_{i-2}, P_{i-1} and P_Γ are used.

$$\sigma = \frac{|x_i - x_\Gamma|}{|x_i - x_{i+1}|} \tag{57}$$

A critical value, σ^*, of this separation parameter is used to decide the stencil taken for one-sided differencing. Two cases are possible:

1. $\sigma \geqslant \sigma^*$: When the grid point P_i has reasonable separation from the marker point P_Γ, it is included in the stencil. Hence, for the example of Fig. 6, a 4th order approximation of the first x derivative of any variable at irregular grid points (P_{i-2}, P_{i-1} and P_i) is obtained by using set of points P_{i-3}, P_{i-2}, P_{i-1}, P_i and P_Γ in Eq. (55).
2. $\sigma < \sigma^*$: When a marker point P_Γ and the nearest interface point P_i are too close to each other, we include P_Γ, but do not use the point P_i in the stencil. In order to maintain the same order of accuracy, an additional grid point, P_{i-4}, from the other end is added to the stencil. In this case, the stencil for the 4th order approximation of the first x derivative of any variable at irregular points consists of P_{i-4}, P_{i-3}, P_{i-2}, P_{i-1} and P_Γ, as shown in Fig. 6. Values at the point P_i, which is dropped from the stencil, are updated by a high-order interpolation from other points of the stencil.

With the appropriate stencils in Fig. 6, values of flow variables at markers and grid points on the low-pressure side of the shock are used to compute derivatives in Eq. (10) at irregular grid points (P_{i-2}, P_{i-1} and P_i). Finite difference approximations on the high-pressure side are found by using values at the high-pressure side of the marker points. Similar to x derivatives, finite difference approximations of derivatives in y direction are calculated using appropriate points along vertical grid lines.

Stability of the high order finite-difference scheme with one-sided differencing at the shock was shown by Zhong [58] on the uniform grid. The stability analysis for the implementation described above is presented in Section 4.5. Based on eigenvalue analysis of the discretization used for fixed-grid shock-fitting and our computational experiments we use $\sigma^* = 1$ for stability. Thus, the nearest grid point to the shock is not used in the stencil and minimum distance between two points in non-uniform stencil is same as the grid spacing. One-sided finite difference is used for irregular points to avoid finite difference stencils crossing the shock front. However, if appropriate jump conditions are known at the shock front, one can use schemes like immersed interface methods (IIM) that find the finite-difference approximation for irregular grid points using a regular stencil with correction terms based on jump conditions. Such methods allow for flow of information across the shocks and can be more accurate if exact jump conditions are enforced. Moreover, the ad hoc parameter σ^* would not be needed. Recently, Zhong [73,78] developed a new immersed interface algorithm that requires jumps only in values of flow variables and their first derivatives while showing arbitrarily high-order accuracy. Since up to first-order jump conditions can be derived from the physics of the problem, this method is more suitable for high-order computations of real problems than other IIM schemes which need higher order derivatives of flow variables to obtain higher order of accuracy. Such IIM schemes should be considered in the future as improvement on the one-sided finite differencing scheme.

4.3. Data structure for marker points at the front and grid points

In addition to the shock front and geometric parameters defined in Section 4.1, the values of flow variables and shock velocity are saved at each marker point. Moreover, data structure is needed to relate marker points on the front with grid points in flow-field. For a two-dimensional grid, there are two types of marker points along the shock front: those at the intersection of the front and a horizontal grid line (ξ-grid line), and those at the intersection with the vertical grid line (η-grid line). Since each marker point is an intersection point, the relation between grid points and marker points is established by storing the type of intersection point (intersecting with ξ-line or η-line) and indices of intersecting gridline for each marker point. Indices of irregular grid points associated with a marker point are also stored with each marker for efficient implementation of one-sided finite difference.

At each grid point, an indicator value, ϕ, is saved to indicate whether the grid point is located at the high pressure or low-pressure side of the shock. There can also be some grid points lying between two interface points where one-sided differencing may not be applied because enough points are not available (Fig. 7). Such points are "skipped" for flux calculations and a unique value of indicator function is assigned to identify such points. Overall, the values of indicator function are defined at every grid point as follows:

$\phi = 1$ for normal points on the low-pressure side.
$\phi = -1$ for normal points on the high-pressure side.
$\phi = 2$ for skipped points on the low-pressure side on a ξ-grid line.
$\phi = -2$ for skipped points on the high-pressure side on a ξ-grid line.
$\phi = 3$ for skipped points on the low-pressure side on an η-grid line.
$\phi = -3$ for skipped points on the high-pressure side on an η-grid line.
$\phi = \pm 4$ for points which do not have enough points in both directions.

For each marker point, the indicator values at its neighboring grid points are checked to see if there are any grid points with $|\phi| > 1$. Since flux values can not be computed at such grid points, these points are updated using interpolations. For a grid point with $|\phi| = 2$, we choose points along the corresponding η-grid line to obtain flow variables at this point by a poly-

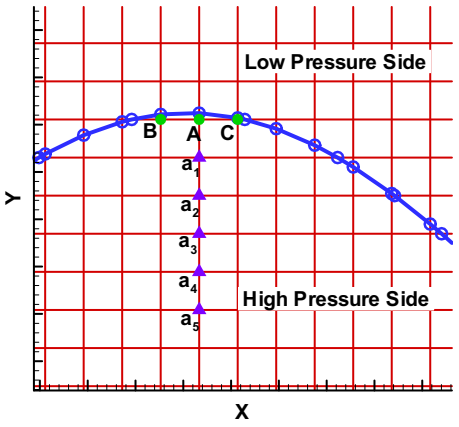

Fig. 7. Treatment of grid points where enough points are not available for taking one-sided difference in x-direction ($\phi = -2$), shown by filled circles. For such points, interpolation is carried out using neighboring grid-points Y-direction, shown by filled triangles.

nomial interpolation. Similarly, neighboring grid points along a ξ-grid line are used in an interpolation at a grid point with $|\phi| = 3$. In Fig. 7, an example is shown of grid point A with $\phi = -2$, which is represented as filled circle. In this case, the grid points shown by filled triangles $(a_1, a_2, \ldots, a_5)$ are used to obtain the flow variables at point A by a polynomial interpolation. The isolated points given by $\phi = \pm 4$ are left out of calculations altogether and can not be handled using one-sided differences. In this case, the grid resolution needs to increase in order to resolve flow variables in this region.

4.4. Shock front velocity

We use the shock-fitting technique of Ref. [58] to obtain an equation of shock acceleration using the Rankine–Hugoniot jump conditions at the shock coupled with characteristic information from the high-pressure side of the flow. In a moving-grid shock-fitting method, the shock is represented as a moving-grid surface of the computational domain. Hence, a shock velocity is related to the grid velocity and metrics of the grid transformation. Since the shock is represented by grid points, flow variable values are readily available for use in finding shock acceleration at the shock points.

In this paper, the conventional shock-fitting method for finding the shock velocity has been extended to the current fixed-grid based shock-fitting method on a fixed grid. This is accomplished through a transformation of the governing equations to the local natural coordinates associated with the local tangential and normal directions to the shock. For computation of the shock velocity at a marker point S_i in Fig. 5, we locally transform the governing equations to a local natural coordinate system $(\xi^*, \eta^*, \zeta^*, \tau^*)$, where η^* represents coordinate in the direction of the shock normal $\vec{\mathbf{n}}$, ξ^* and ζ^* coordinates are aligned in tangential directions, and $\tau^* = t$ is the time variable for the transformed coordinate system. Orthogonal transformation of the governing equations is carried out from the physical coordinates to the local natural coordinates as

$$\begin{bmatrix} \xi^* - \xi^*_s \\ \eta^* - \eta^*_s \\ \zeta^* - \zeta^*_s \\ \tau^* \end{bmatrix} = \begin{bmatrix} \tau_{1x} & \tau_{1y} & \tau_{1z} & 0 \\ n_x & n_y & n_z & 0 \\ \tau_{2x} & \tau_{2y} & \tau_{2z} & 0 \\ 0 & 0 & 0 & 1 \end{bmatrix} \begin{bmatrix} x - x_s \\ y - y_s \\ z - z_s \\ t \end{bmatrix} \tag{58}$$

where $\vec{\mathbf{n}}$ represents the shock normal unit vector at the given point S_i, and $\vec{\tau_1}$ and $\vec{\tau_2}$ are tangential unit vectors. The component τ_{1x} in the transformation matrix above is the directional cosine of the local unit vector $\vec{\tau_1}$, with respect to the x-axis. The other components of the matrix can be defined similarly. The coordinates of marker point S_i in the local natural coordinate system are $(\xi^*_s, \eta^*_s, \zeta^*_s)$, and those in the physical coordinate system are (x_s, y_s, z_s).

With the transformation to the local natural coordinate system, one can directly use the moving-grid shock-fitting method of Ref. [58]. Following the relations given by Zhong [58], we obtain the following relation for the shock acceleration:

$$\begin{aligned} &\frac{\partial v_n}{\partial t} = \frac{1}{[\mathbf{I}_N \cdot (\mathbf{U_s} - \mathbf{U_0})]} \left[(u_{ns} - v_n + c_s)\mathbf{I}_N \cdot \left(\frac{\partial \mathbf{U}}{\partial \tau^*}\right)_s + \mathbf{I}_N \cdot (\mathbf{F_s} - \mathbf{F_0}) \cdot \frac{\partial \mathbf{a}}{\partial \tau^*} - \mathbf{I}_N \cdot \left(\frac{\partial \mathbf{F_0}}{\partial \tau^*} \cdot \mathbf{a} + \frac{\partial \mathbf{U_0}}{\partial \tau^*} \cdot v_n \right) \right] \\ &\mathbf{a} = n_x \hat{i} + n_y \hat{j} + n_z \hat{k} \\ &\left(\frac{\partial \mathbf{U}}{\partial \tau^*}\right)_s = \left(\frac{\partial \mathbf{U}}{\partial t}\right)_s - v_n \left\{ \mathbf{n}_x \left(\frac{\partial \mathbf{U}}{\partial x}\right)_s + \mathbf{n}_y \left(\frac{\partial \mathbf{U}}{\partial y}\right)_s + \mathbf{n}_z \left(\frac{\partial \mathbf{U}}{\partial z}\right)_s \right\} \end{aligned} \tag{59}$$

Here, v_n is the shock normal velocity and u_{ns} is the normal component of flow velocity on the high-pressure side of the shock. $\mathbf{I}_N$ is the left eigenvector for the characteristic field approaching the shock from behind with a velocity (eigenvalue) of $(u_{ns} - v_n + c_s)$. Conservative flow variables represented by $\mathbf{U}$ and flux vectors $\vec{\mathbf{F}} = E\hat{i} + F\hat{j} + G\hat{k}$ have the same form as given by Eqs. (5)–(8). Subscripts 's' and '0' are used to denote the high pressure and low-pressure sides of the shock respectively.

The values of the fluxes, flow variables, and their spatial derivatives at the marker point are obtained by high-order polynomial interpolations. Thus along with the Navier–Stokes equations, one needs to solve the following system of equations:

$$\begin{aligned}\frac{\partial v_n}{\partial \tau} &= f\left(x_s, y_s, \mathbf{U_s}, \mathbf{U_0}, l_N \cdot \frac{\partial \mathbf{U_s}}{\partial \tau}, v_n\right)\\ \frac{\partial x_s}{\partial \tau} &= v_n n_x\\ \frac{\partial y_s}{\partial \tau} &= v_n n_y\end{aligned} \tag{60}$$

The locations of all marker points and the shock shape are updated with time by solving Eq. (60) by a Runge–Kutta scheme. From one time step to the next, a new set of intersection points with the grid lines are recalculated by using a Newton–Raphson iteration procedure. Subsequently, the geometric properties of the shock and the shock data structure are also updated. As the shock-front moves from one time step to the next, it can cross some grid points as highlighted by the circles in Fig. 8. As a result, the value of the indicator ϕ changes sign and the flow variables at such grid points will experience a discontinuous transition from one side of the shock to another. Current algorithm checks for these "crossed" grid points after every time step and corrects the value of the indicator ϕ. New flow variable values at these points are corrected to those of the other side of the shock by a polynomial interpolation. The stencil for the polynomial interpolation is chosen by taking closest grid points with same ϕ value. The procedure is similar to updating $|\phi| > 1$ points as described in Section 4.3.

In this paper, Eq. (60) is advanced in time by Runge–Kutta schemes of up to third-order accuracy. As an example, an algorithm with the first-order Euler method of time stepping is shown below:

General Algorithm:

0. Set initial conditions of flow-field variables and interface data.
1. Find one-sided difference coefficients for the irregular points.
2. Find fluxes at all the grid points, including regular and irregular points.
3. Compute the right hand side of shock acceleration relation in Eq. (60).
4. Update values of flow variables from the calculated fluxes to obtain $\mathbf{U}^{n+1}$ at all regular grid points as well as irregular grid points where $|\phi| = 1$ and $\sigma \geqslant \sigma^*$.
5. Compute new shock-front locations and velocities, and make necessary corrections due to shock movement across the grids:
   a. Update $\mathbf{U}^{n+1}$ at grid points where $\sigma < \sigma^*$.
   b. Update $\mathbf{U}^{n+1}$ at grid points where $|\phi| > 1$.
   c. Update shock velocities for all interface points and the coordinates of the previous marker points at time step $n + 1$.
   d. Obtain new marker points at the intersection of the new shock shape with the grid lines.
   e. Identify and update the grid points that are crossed by the shock movement.
   f. Update the data structure relating grid points and markers.
6. Advance time $t^{n+1} = t^n + \Delta t$.
7. Obtain flow-field values at the low-pressure (supersonic) side of the marker points from a one-sided interpolation.
8. Use the Rankine–Hugoniot relations to obtain values on the high-pressure (subsonic) side of the marker points.

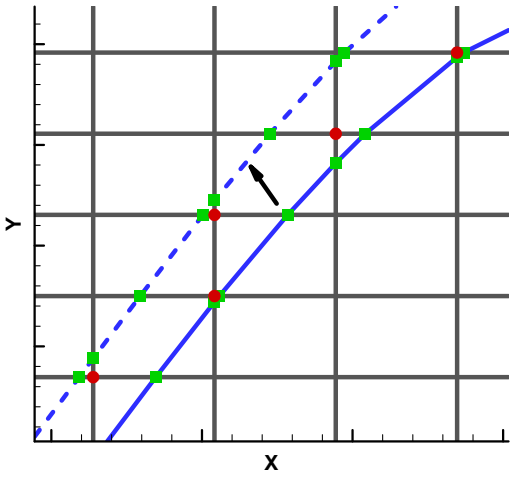

Fig. 8. Grid points crossed (highlighted by filled circles) by movement of shock-front from old position from (solid line), to a new position (dashed line). New values at such grid points are required as they are on wrong side of the shock due to shock movement.

9. Apply boundary conditions of the computational domain.
10. If $t < t_{end}$, go back to step 1.

4.5. Stability of the finite-difference schemes used

In the shock reference frame, the flow in low-pressure side moves towards the shock at supersonic speeds. Hence, flow variables on low pressure side of the shock are determined completely by the upstream conditions without needing any information from the shock. The flow in the high-pressure side of the shock is subsonic in the shock reference frame. Hence, from the flow behind the shock wave one characteristic wave should move towards the shock front while other information needed to determine flow variables should come from the conservation laws in form of Rankine Hugoniot jump conditions. As described in Section 3.1, a typical shock-fitting method uses an appropriate characteristic compatibility relation (Eq. (22)) along with Rankine Hugoniot jump conditions (Eqs. (13), (14) and (24)) to arrive at the expression of shock velocity (Eq. (26)). Using these values of shock velocity, values of flow variables on the high-pressure side of the shock are computed using Rankine–Hugoniot conditions. Thus, shock-fitting method provides coupling between the low-pressure and high-pressure sides of the shock, which is consistent with physical laws of conservation of fluxes and propagation of characteristic waves in compressible flows. Values of flow variables thus computed at the shock point are used as boundary conditions just like any other method. In essence, use of shock-fitting methods is similar to solving wave equations with a characteristic boundary condition. However, one needs to make sure that the implementations for finite-difference schemes on either side of the shock do not become unstable. Stability and development of our regular 5th-order upwind scheme has been discussed in great detail in Ref. [58] using an eigenvalue analysis of the semidiscretized equations. Here we extend the analysis by using one sided irregular stencils as described in Section 4.2. Other options for the stability analysis could be energy methods [79] and Laplace transforms [80,81]. One of the popular stability theories using Laplace transforms is given by Gustafsson et al. [81]. However, some high-order schemes that are stable by criteria of Ref. [81] are not asymptotically stable [82]. We prefer the numerical stability analysis of eigenvalue spectra of semidiscretized equations because it is a simple and effective approach which ensures asymptotic stability of a finite-difference scheme coupled with boundary treatments.

The model equation of the inviscid Euler equations is the linear wave equation

$$\frac{\partial u}{\partial t} = -c\frac{\partial u}{\partial x} \tag{61}$$

With our Front-Tracking method, the wave equation is solved using interface point along with the grid points. We can assume arrangement shown in Fig. 9 of these points without loss of generality.

In the implementation of shock-fitting method, some characteristic waves exit at the shock boundary while some characteristics enter through the shock front in the computational domain. Hence, we will consider two set-ups for linear stability analysis with grids shown in Fig. 9:

$c > 0$: interface at point 1 is inlet of the wave and upwind scheme is used in interior.
$c < 0$: interface at point 1 is exit of the wave and downwind scheme is used in interior.

Consider first, a spatial discretization of Eq. (61) using a fifth-order upwind scheme for $c > 0$. In this case, Dirichlet boundary condition is used at point 1, i.e., $u(x_1, t) = u_1(t)$ is specified. Characteristic boundary condition at the exit point NL amounts to computing spatial derivative u'_{NL} at exit using the one-sided 4th order difference equation. Using the upwind finite-difference scheme on the regular grid points (described by Eq. (39)) and one-sided difference at irregular points (described by Eq. (45)), one obtains following system of equations:

$$\begin{cases} u'_i = \sum_{j\in \mathbf{I}_n} l_j^{n'}(x_i)u(x_j) \quad (i = 2,3,4) \\ u'_i = \frac{1}{b_0 h}\sum_{k=-3}^{3} a_k u_{i+k} \quad (i = 5,6,\ldots,NL-3) \\ u'_{NL-2} = \frac{1}{b_0 h}(5u_{NL-4} - 40u_{NL-3} + 40u_{NL-1} - 5u_{NL}) \\ u'_{NL-1} = \frac{1}{b_0 h}(-5u_{NL-4} + 30u_{NL-3} - 90u_{NL-2} + 50u_{NL-1} + 15u_{NL}) \\ u'_{NL} = \frac{1}{b_0 h}(15u_{NL-4} - 80u_{NL-3} + 180u_{NL-2} - 240u_{NL-1} + 125u_{NL}) \end{cases} \tag{62}$$

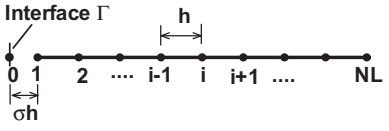

Fig. 9. Uniform grid with interface representing a boundary of the computational domain considered for stability analysis of wave Eq. (61).

Here, u_i' is the discretization of $\partial u(x_i,t)/\partial x$. $l_j^n(x)$ is the jth Lagrange basis polynomial on a set of points $\mathbf{I}_n = \{1,2,3,4,5\}$ as described in Section 4.2. As discussed for Eq. (39) $a_{\pm 3} = \pm 1 + \alpha/12$, $a_{\pm 2} = \mp 9 - \alpha/2$, $a_{\pm 1} = \pm 45 + 5\alpha/4$, $a_0 = -5\alpha/3$ and $b_0 = 60$. The scheme is upwind when $\alpha < 0$ and downwind when $\alpha > 0$. Following recommendation in Ref. [58] we use $\alpha = -6$ for the upwind scheme and $\alpha = 6$ for the downwind scheme. The system of Eqs. (62) can be written in following form

$$\frac{d\mathbf{U}}{dt} = \mathbf{A}\mathbf{U} + \mathbf{g}(t) \tag{63}$$

where $\mathbf{U} = (u_2,\ldots,u_{NL})^T$ and $\mathbf{g}(t) = -c\left(l_1^{n'}(x_2)u_1,\ l_1^{n'}(x_3)u_1,\ l_1^{n'}(x_4)u_1,\ 0,\ \ldots,\ 0\right)^T$. The asymptotic stability condition for the semi-discrete equations is that all the eigenvalues of the matrix $\mathbf{A}$ should contain no positive real parts. Matrix $\mathbf{A}$ for the upwind case is

$$\mathbf{A} = -\frac{c}{hb_0}\begin{bmatrix}
\chi_{22} & \chi_{23} & \chi_{24} & \chi_{25} & & & & & \\
\chi_{32} & \chi_{33} & \chi_{34} & \chi_{35} & & & & & \\
\chi_{42} & \chi_{43} & \chi_{44} & \chi_{45} & & & & & \\
a_{-3} & a_{-2} & a_{-1} & a_0 & a_1 & a_2 & a_3 & & \\
 & \cdot & \cdot & \cdot & \cdot & \cdot & \cdot & \cdot & \\
 & & a_{-3} & a_{-2} & a_{-1} & a_0 & a_1 & a_2 & a_3 \\
 & & & & 5 & -40 & 0 & 40 & -5 \\
 & & & & -5 & 30 & -90 & 50 & 15 \\
 & & & & 15 & -80 & 180 & -240 & 125
\end{bmatrix} \tag{64}$$

Here, $\chi_{ij} = hb_0 l_j^{n'}(x_i)$ and $(i,j \in \mathbf{I}_n)$. Eigenspectra for this matrix with $c = h = 1.0$ and $NL = 51$ is presented in Fig. 10(a) for three different values of σ. It is observed that all the eigenvalues of the spatial discretization matrix are negative for all the considered values of σ in the present study. In our numerical experiments with different number of total grid points, real parts of all the eigenvalues were always found to be negative. For the results presented in this study, σ remains between 1.0 and 2.0. Hence, the implementation of finite-difference method is stable for the upwind waves.

Similar to the case of the upwind wave, stability of the method can also be tested for the downwind waves ($c < 0$ on the grid of Fig. 9). For this case $\alpha = 6.0$ and values at point NL needs to be specified while values at point 1 are computed. Discretization leads to the system of equations represented by Eq. (63) with $\mathbf{U} = (u_1,\ldots,u_{NL-1})^T$ and $\mathbf{g}(t) = -c/hb_0\ (0,\ldots,a_3u_{NL}, -5u_{NL} - 1, 15u_{NL})^T$. Matrix $\mathbf{A}$ for corresponding to the downwind wave is given by

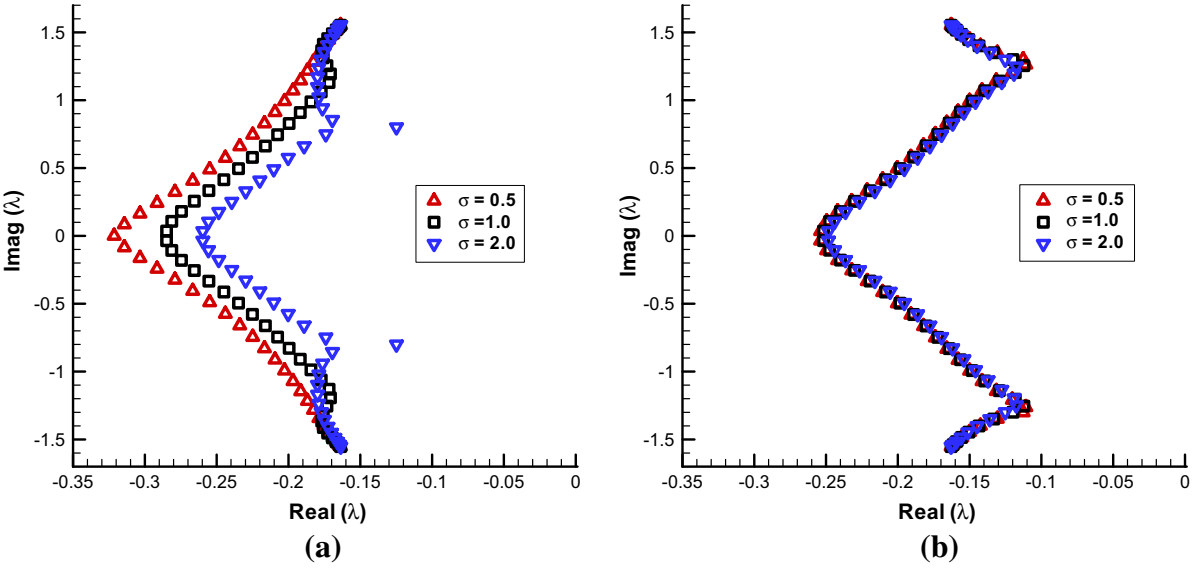

Fig. 10. Eigenvalue spectra for fifth order upwind scheme applied on irregular grid of Fig. 9 with several values of σ. (a) Upwind scheme, $c > 0$, $\alpha = -6$ and (b) downwind scheme, $c < 0$, $\alpha = 6$.

$$\mathbf{A} = -\frac{c}{hb_0}\begin{bmatrix}
\chi_{11} & \chi_{12} & \chi_{13} & \chi_{14} & \chi_{15} & & & & & & \\
\chi_{21} & \chi_{22} & \chi_{23} & \chi_{24} & \chi_{25} & & & & & & \\
\chi_{31} & \chi_{32} & \chi_{33} & \chi_{34} & \chi_{35} & & & & & & \\
\chi_{41} & \chi_{42} & \chi_{43} & \chi_{44} & \chi_{45} & & & & & & \\
 & a_{-3} & a_{-2} & a_{-1} & a_0 & a_1 & a_2 & a_3 & & & \\
 & & \cdot & \cdot & \cdot & \cdot & \cdot & \cdot & \cdot & \cdot & \\
 & & & & a_{-3} & a_{-2} & a_{-1} & a_0 & a_1 & a_2 & a_3 \\
 & & & & & a_{-3} & a_{-2} & a_{-1} & a_0 & a_1 & a_2 \\
 & & & & & & & 5 & -40 & 0 & 40 \\
 & & & & & & & -5 & 30 & -90 & 50 \\
 & & & & & & & 15 & -80 & -180 & -240
\end{bmatrix}. \tag{65}$$

Eigenspectra of Matrix **A** for downwind wave with $c = -1.0$, $h = 1.0$ and $NL = 51$ is plotted in Fig. 10(b). It can be observed that all eigenvalues are negative for the three values of σ considered here. This was found to be true irrespective of number of total points chosen in the grid-set.

For the results presented in this paper, σ is between 1.0 and 2.0 and we can see that the implementation of finite-difference scheme remains stable for these values. Overall, it is observed that the implemented method is stable for the waves either entering the computational domain through the interface or exiting through it. Asymptotic stability of the discretizations considered here imply that using method of lines and higher order Runge Kutta (RK-3 in our case) time stepping with appropriate CFL numbers should lead to stable solutions.

5. Order of accuracy evaluation of shock-fitting methods

There have been very few studies evaluating the order of accuracy of numerical schemes for compressible flow with nonlinear discontinuities like shocks. Casper and Carpenter [66,83] simulated shock–disturbance interaction problems using a shock-capturing scheme and found only first-order convergence in the smooth post-shock flow, even with a high order scheme. In general, shock-capturing methods suffer from a reduction in accuracy in the post-shock flow fields. Hence, it is important to ensure that design accuracy is achieved with a high-order shock-fitting method for shock–disturbance interaction problems. Suresh [84] investigated the grid convergence of a third-order shock-fitting method in computing a one-dimensional shock-entropy wave interaction problem. His shock-fitting method is different from those considered in this paper, since it is based on adding new grids instead of moving the grid points as the shock moves. Moreover, in the method used by Suresh [84], the governing equations are solved in primitive variables, Riemann problem is solved to find the shock-velocity and values of all the flow variables at the shock points are obtained by extrapolations from the interior. On the other hand, we solve the equations in conservative form with an option of using shock-capturing scheme and consider various different methods of computing shock velocity as shown in Table 1. The flow considered by Suresh is a modified form of the popular Shu–Osher problem [85], such that the solution is smooth behind the main shock. In this paper, we use the same flow to test the numerical accuracy of various shock-fitting schemes listed in Table 1.

Specifically, we consider a one-dimensional shock interaction with an incoming entropy wave represented by density disturbances in front of the shock in the following form:

At $t = 0$ for $0 \leqslant x \leqslant 2.0$

$$\begin{aligned}
\rho &= (\gamma+1)M^2/[(\gamma-1)M^2+2] \\
u &= \gamma^{1/2}[2(M^2-1)/\{(\gamma+1)M\} - M] \\
p &= 1 + 2\gamma(M^2-1)/(\gamma+1)
\end{aligned} \tag{66}$$

while for $x > 2.0$ and $t \geqslant 0$,

$$\begin{aligned}
\rho_\infty &= 1.0 + \varepsilon \sin^4\{2.5\pi(x + M\gamma^{1/2}t)\} \\
u_\infty &= -M\gamma^{1/2} \\
p_\infty &= 1.0
\end{aligned} \tag{67}$$

where ρ, γ, u, M and p represent density, ratio of specific heats, velocity, Mach number and pressure, respectively. The shock is initially located at $x = 2.0$ and shock-fitting methods compute the flow behind the shock only. The mean Mach number of the shock is $M = 3$. The other parameters of the flow are: $\gamma = 1.4$, $\varepsilon = 0.2$. The entropy waves given by Eq. (67), which were used by Suresh [84], are smoother than those used by Shu and Osher [85], so that solution after the shock is continuous for up to third derivatives. The unsteady problem is computed until $t = 0.32$ for all results presented in this paper, so that shocklets are not formed behind the main shock. Thus, the problem is expected to show the true order of convergence for a shock-fitting method.

To carry out the convergence analysis, we compute the unsteady flow with three sets of different grid sizes:

$$\begin{aligned} &\text{Grid I}: \Delta x_1 = 2.5 \times 10^{-3} \ (N = 800) \\ &\text{Grid II}: \Delta x_2 = 1.25 \times 10^{-3} \ (N = 1600) \\ &\text{Grid III}: \Delta x_3 = 6.25 \times 10^{-4} \ (N = 3200) \end{aligned} \tag{68}$$

An extra solution is also obtained by using Method A-u with a very fine grid ($\Delta x = 1.5625 \times 10^{-4}$) and is served as a reference "exact" solution. The error values are obtained for different sets of grids and the approximate order of accuracy, n, is then computed by:

$$n = \log\left(\frac{e_{\Delta x}}{e_{\Delta x/2}}\right) \Big/ \log(2) \tag{69}$$

Here, e_h represents an error for grid spacing h from the reference "exact" solution.

5.1. Effects of different methods of computing shock velocities

We first compare the accuracy of Methods A-u, B-u, and C-u (defined in Table 1) for the effects of different methods of computing the shock velocities. In the interior of the flow field, these three methods use the same fifth-order upwind central differencing scheme of Zhong [58] in space and a RK-3 time-stepping methods in time.

5.1.1. Method A-u

Method A-u described in Section 3.1.1 and Ref. [58], is the conventional shock-fitting method where the shock is updated using a shock acceleration relation based on the Rankine–Hugoniot conditions and one characteristic relation behind the shock. Solutions from all three sets of grids obtained with this method are compared against the reference solution in Fig. 11. It can be observed that the results are fairly indistinguishable from each other in full view. As we zoom in on the different portions of the density profiles, it is noticed that results are converging with grid refinement in Fig. 11(b). Error values for Method A-u are presented in Table 2. It can be seen that approximately fifth-order convergence is observed for the conventional moving-grid shock-fitting Method A-u.

5.1.2. Method B-u

Method B-u uses an alternative relation for shock acceleration obtained by using a momentum equation instead of a characteristic relation, as done by Henrick [68] (see Table 1). The results obtained from Method B-u are compared with those of the conventional Method A-u for Grid I in Fig. 12. The results obtained from Method A-u match significantly better to the reference solution as compared to those from Method B-u.

The error values for Method B-u are quantified in Table 3. The table shows that Method B-u does not reach the expected nominal 5th-order accuracy. Instead, an order of 2.3 is obtained for Method B-u based on the results of cases of Grid II and Grid III.

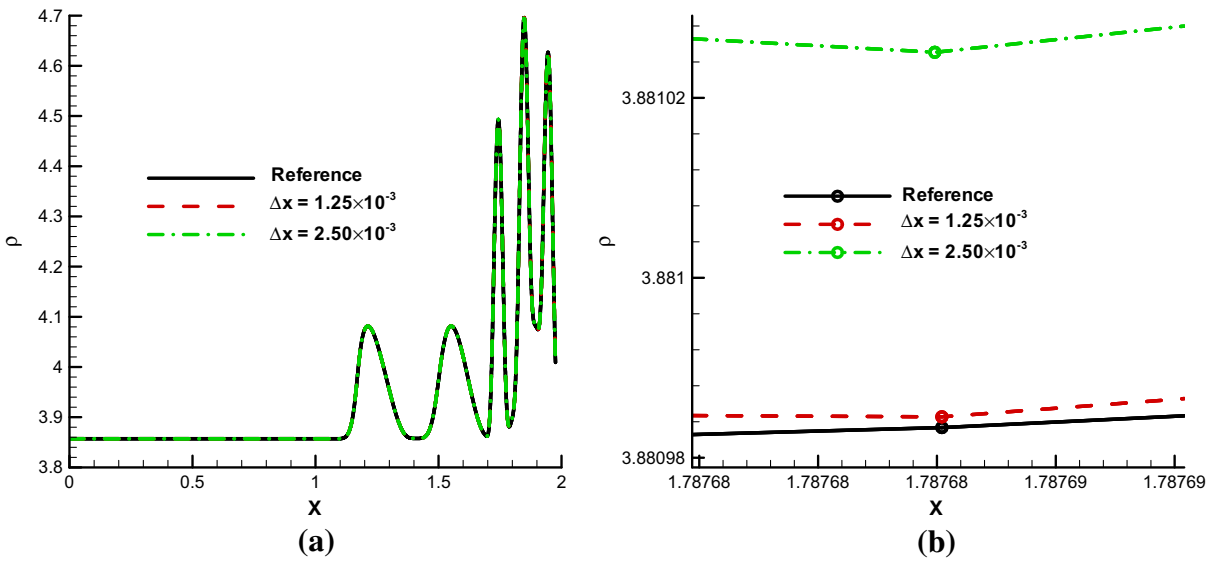

Fig. 11. (a) Density variation for the shock–disturbance interaction problem obtained from Method A-u for three sets of grids and (b) zoomed view of the density profile near the contact discontinuity.

Table 2
L-1 errors from Method A-u (conventional shock-fitting) for problem defined by (66) and (67).

	Grid I $e_{\Delta x_1}$	Grid II $e_{\Delta x_2}$	Grid III $e_{\Delta x_3}$	Order from I and II	Order from II and III
Density	1.02E−05	4.39E−07	1.63E−08	4.541	4.747
Velocity	7.77E−07	2.43E−08	7.89E−10	4.999	4.945
Pressure	5.87E−06	1.89E−07	6.06E−09	4.958	4.961

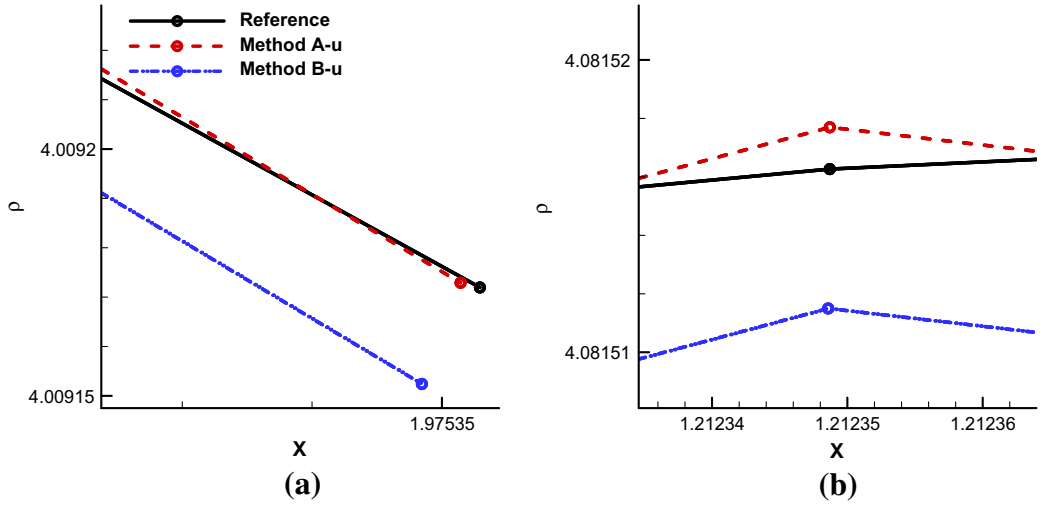

Fig. 12. Comparison of density variation between Methods A-u and B-u, and the reference solution: (a) and (b) represent zoomed portions near and away from the shock, respectively. ($\Delta x = 2.5 \times 10^{-3}$).

Table 3
L-1 errors of Method B-u.

	Grid I $e_{\Delta x_1}$	Grid II $e_{\Delta x_2}$	Grid III $e_{\Delta x_3}$	Order from I and II	Order from II and III
Density	9.66E−06	7.40E−07	1.60E−07	3.706	2.208
Velocity	2.00E−06	1.58E−07	3.24E−08	3.659	2.291
Pressure	1.58E−05	1.25E−06	2.54E−07	3.653	2.305

As pointed out by one of the reviewers, it is important to test if Method A-u and Method B-u are converging to the same solution as we refine the grid. To this end, we computed a fine grid solution using Method B-u with same grid spacing as the reference solution ($\Delta x = 1.5625 \times 10^{-4}$). The L-1 errors for this solution in density, velocity, and pressure were found to be 9.83×10^{-9}, 1.99×10^{-9}, and 1.55×10^{-8}, respectively. These error values are more than an order smaller than the errors tabulated in Table 3. It was indeed found that the error values do not change significantly when fine grid results from Method B-u is used instead of those from Method A-u as the reference solutions.

Thus, as compared to Methods A-u, Method B-u leads to higher errors when the shock is updated using the momentum equation. Moreover, as the grid is refined, the rate of convergence is less than the expected 5th order of accuracy. Shock velocity and jump conditions across a shock wave in a shock-fitting algorithm should be compatible with the physics of the problem as well as numerically stable. The flow behind the shock is subsonic. As shock is used as an inflow boundary only one characteristic is needed from the flow behind the shock. Method A-u uses this characteristic relation directly, while Method B-u replaces this by use of the momentum equation. We observe in our implementations that the shock acceleration method which uses the characteristic relation gives more accurate results than the method using only a momentum equation.

5.1.3. Method C-u

Method C-u does not use a shock acceleration equation to compute the shock velocity. In this method, shock velocities are obtained directly from a Riemann invariant, similar to some earlier studies [86]. Like Methods A-u and B-u, a fifth-order upwind finite-difference method is used in space (see Table 1) and a RK-3 scheme is used in time.

The density profiles for the three sets of grids computed by Method C-u are presented in Fig. 13 and compared to the reference profile. As we zoom on a portion away from the shock (Fig. 13(a)), we see that the results are converging towards the reference values with grid refinement. In Fig. 13(b), the effect of grid refinement on the prediction of shock location is shown.

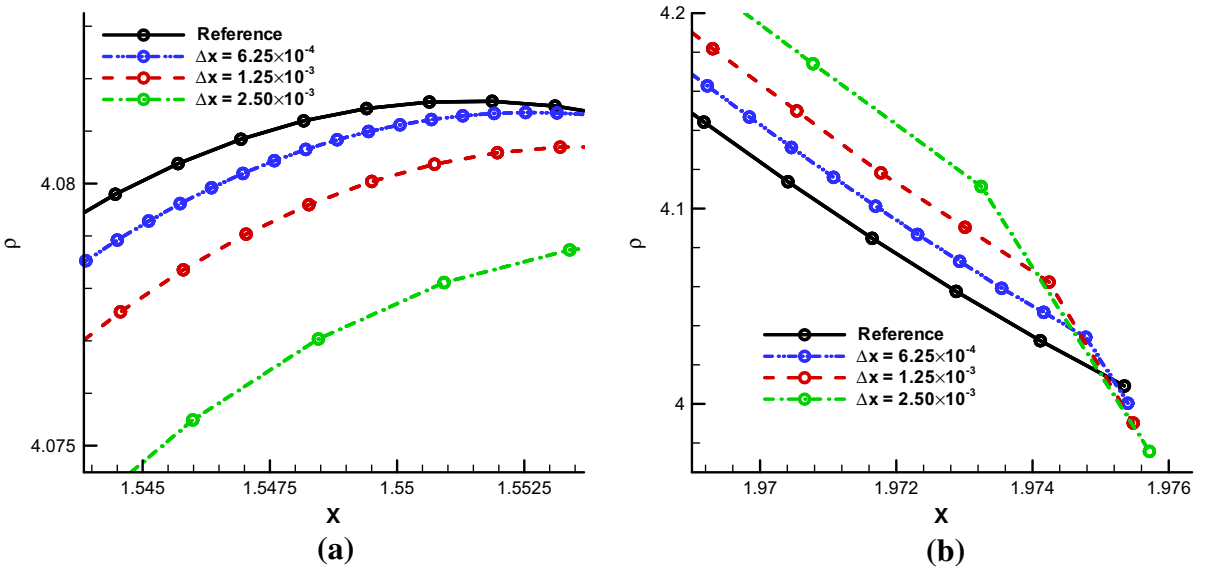

Fig. 13. Density variation for the smoother version of the Shu–Osher problem for different grid sets using Method C-u: (a) and (b) are zoomed versions of the profile showing convergence.

We observe for all the three sets of grids used in this study, a sudden jump in density from the shock point to the adjacent grids points after the shock. Such a jump is not observed in the solutions of Methods A-u and B-u, which advance the shock based on shock acceleration formulas. Nevertheless, Fig. 13(b) shows that the shock location computed by Method C-u converges towards the reference value as the grid is refined.

Computational order of accuracy for Method C-u is presented in Table 4. This method seems to be only first-order accurate. In addition, the errors of Method C-u are about three orders of magnitudes larger for Grid II than those obtained by Method A-u. Thus, Method C-u of determining shock velocity based on a Riemann invariant results in poor accuracy as compared to those obtained from the shock acceleration formulations of Methods A-u and B-u. A possible reason for the sudden jump in density profiles at the shock is the inconsistency between flow variables behind the shock computed by the Riemann invariant and those computed by the local Euler equations. On the other hand, Methods A-u and B-u, which determine the movement of the shock based on the shock acceleration, ensure that changes in shock velocity are smoother and, thus, show expected order of convergence.

To summarize, we find that the conventional shock-fitting Method A-u of advancing the shock using the characteristics based shock acceleration relation is most accurate for the unsteady shock disturbance interaction problems considered. It maintains the expected 5th order accuracy of the numerical method. On the other hand, Method B-u has higher errors and has lower order of accuracy. Method C-u is simple in implementation, but is only first-order accurate and several orders of magnitude larger in computational errors in the test cases computed.

It should be noted, however, that convergence of Methods B-u and C-u is not in question here. The results show that the Methods B-u and C-u do converge to the same solution as Method A-u. The exact reason for the slight reduction in accuracy of order for Methods B-u and C-u is not known. Our best explanation for lower order of accuracy of these two methods is that there is slight discrepancy between physics of the flow and the numerical implementation at the shock.

Method C-u was found to be only first-order accurate and performed worse than the Methods A-u and B-u. Shock velocity in Methods A-u and B-u is found by solving shock acceleration relations. Shock velocity equations along with conservative approximation of Euler equations form system of linear equations which is solved consistently while, for Method C-u, shock velocity enters as a boundary condition. Methods A-u and B-u use conservative fluxes while the Method C-u computes the shock velocity based on interpolation of flow variables without using values of fluxes. In our understanding, this results in slight inconsistency between flow variables behind the shock computed by the Riemann invariant and those computed by the local Euler equations.

Table 4
L-1 errors using Method C-u.

	Grid I $e_{\Delta x_1}$	Grid II $e_{\Delta x_2}$	Order from I and II
Density	5.69E−03	3.32E−03	0.7777
Velocity	1.23E−03	6.97E−04	0.8188
Pressure	9.57E−03	5.46E−03	0.8105
Shock location	3.68E−04	1.30E−04	1.5023

In our opinion, difference between the numerical orders of accuracy from Methods B-u and A-u is due to the fact that method B-u considers only the normal momentum equation behind the shock to find the shock acceleration relation while A-u uses the compatibility relation corresponding to the characteristic wave coming from behind the shock. Moreover, in Method A-u values of fluxes on upstream and downstream side of the shock front are enforced to be equal (Eq. (24)). Hence, the fluxes from upstream side of the shock enter the shock acceleration relation of Method A-u (Eq. (26)). In the Method B-u, velocity flux from downstream of the shock is considered but no upstream fluxes are used in shock acceleration relation (31). Hence, our opinion is that Method A-u is better aligned with physics of the problem as compared to Methods B-u or C-u, and thus leads to slightly better results.

5.2. Effects of different algorithms for spatial derivatives in shock-fitting methods

In a shock-fitting method, shock-advancing algorithms considered in Section 5.1 can be combined with any algorithm for approximating spatial derivatives in the governing equations. Conventional shock-advancing Method A-u coupled with a 5th-order upwind finite-difference scheme gives nominal high-order convergence rates if the flow behind the shock is smooth enough. However, the high-order upwind scheme is not suitable if secondary shocks are present behind the fitted main shock. Since the secondary shocklets can exist in a flow field of a shock–turbulence interaction problem, it is important to consider shock capturing schemes to solve the post-shock flow, while the main shock is still fitted. It should be noted that the choice of using shock capturing scheme behind shock fitting have to be made beforehand. If shocklets behind the main shock is expected we should use shock capturing scheme with shock-fitting algorithm.

It should be noted that questions may arise about the stability of WENO schemes using one sided finite-difference around the fitted shocks. We use this approach as near a boundary of the computational domain, all the points needed for usual application of WENO scheme are not available. This problem, however, is universal to any implementation of the WENO schemes, in both shock-capturing and shock-fitting methods, as long as a non periodic boundary is involved. We simply use the commonly used approach to treat boundary condition for the WENO schemes at the boundary points. An alternative way to treat the boundary is to reduce the order at the boundary and use lesser points in the stencil. We choose to use an implementation which has been successfully used in the literature [68] since it allows treatment of boundary without reducing the global order. For smooth flows close to the shock, stability of the optimal WENO stencil can be shown with the boundary conditions presented here. It is possible that shocklets too close to the shock might cause problems for these WENO implementations but shock-fitting method itself is not well suited if shocklets interact with the shock. Some ad hoc measures (like adaptively refining the grid near the shock) can be used to avoid shocklets moving to the fixed stencil portion of the stencil. The method is still very useful if the shocklets appear far downstream of the shock. Moreover, application of WENO schemes with shock-fitting has utility in mutli-component flow downstream of the shock. Such implementations have been previously used for study of detonations [68] and we expect them to be useful for study of many applications including interaction of turbulence with normal shocks. Hence, we believe it is valuable to analyze convergence properties of such methods.

For grid-convergence study, we solve the shock–disturbance interaction problem defined by Eqs. (66) and (67) using combined shock-fitting and shock-capturing schemes (Methods A-w1, A-w2, A-w3, and A-w4 in Table 1). We compare the results with those obtained from the Method A-u. For the purpose of comparison, we also evaluate the accuracy of a pure WENO5 scheme, which captures the main shock without fitting it.

Table 5 shows L-1 errors in density values computed by various schemes with three sets of grids. It can be observed that the computational accuracy of Methods A-w1 and A-w3 do not differ significantly from those of Methods A-w2 and A-w4, respectively. Thus, the choice of one-sided difference schemes, i.e., Eq. (49) or (50) for the points immediately behind the shock boundary does not significantly alter the errors in flow density. However, a comparison of the error values for Methods A-w1 and A-w3 suggests that WENO5M produces significantly smaller errors than WENO5 does. As described in Section 3.2.2, WENO5M maps weights calculated in the WENO5 scheme to the values that are closer to ideal weights for 5th-order accuracy. Thus, in a smooth region of the flow field, WENO5M leads to smaller errors. The errors of all WENO schemes for Methods A-w1 to A-w4, however, are at least three times as large as those of the fifth-order upwind difference scheme used in Method A-u. It can also be observed that for all four WENO schemes coupled with a shock-fitting method, the solutions approach to the nominal accuracy of 5th order as grid is refined. Similar observations are made in Table 6, when grid convergence of velocity field is studied. However, errors in velocities are affected by the choice of one-sided difference schemes

Table 5
L-1 errors and grid convergence of density using various shock-fitting schemes and a pure shock-capturing WENO scheme.

	Grid I: $e_{\Delta x_1}$	Grid II: $e_{\Delta x_2}$	Grid III: $e_{\Delta x_3}$	Order from I and II	Order from II and III
Upwind FD: Method A-u	1.02E−05	4.39E−07	1.63E−08	4.541	4.747
WENO5: Method A-w1	1.04E−04	8.35E−06	3.00E−07	3.634	4.798
WENO5: Method A-w2	1.04E−04	8.36E−06	3.04E−07	3.643	4.782
WENO5M: Method A-w3	3.33E−05	2.17E−06	4.55E−08	3.938	5.578
WENO5M: Method A-w4	3.40E−05	2.18E−06	4.61E−08	3.967	5.560
Pure WENO5	5.31E−03	2.67E−03	1.26E−03	0.994	1.080

Table 6
L-1 errors and grid convergence of velocity using various shock-fitting schemes and a pure shock-capturing WENO scheme.

	Grid I: $e_{\Delta x_1}$	Grid II: $e_{\Delta x_2}$	Grid III: $e_{\Delta x_3}$	Order from I and II	Order from II and III
Upwind FD: Method A-u	7.77E−07	2.43E−08	7.89E−10	4.999	4.945
WENO5: Method A-w1	2.92E−06	1.21E−07	4.56E−09	4.595	4.727
WENO5: Method A-w2	3.78E−06	1.55E−07	5.90E−09	4.606	4.717
WENO5M: Method A-w3	1.13E−06	3.70E−08	1.29E−09	4.928	4.837
WENO5M: Method A-w4	1.44E−06	4.73E−08	1.69E−09	4.925	4.809
Pure WENO5	2.84E−03	1.55E−03	7.14E−04	0.871	1.118

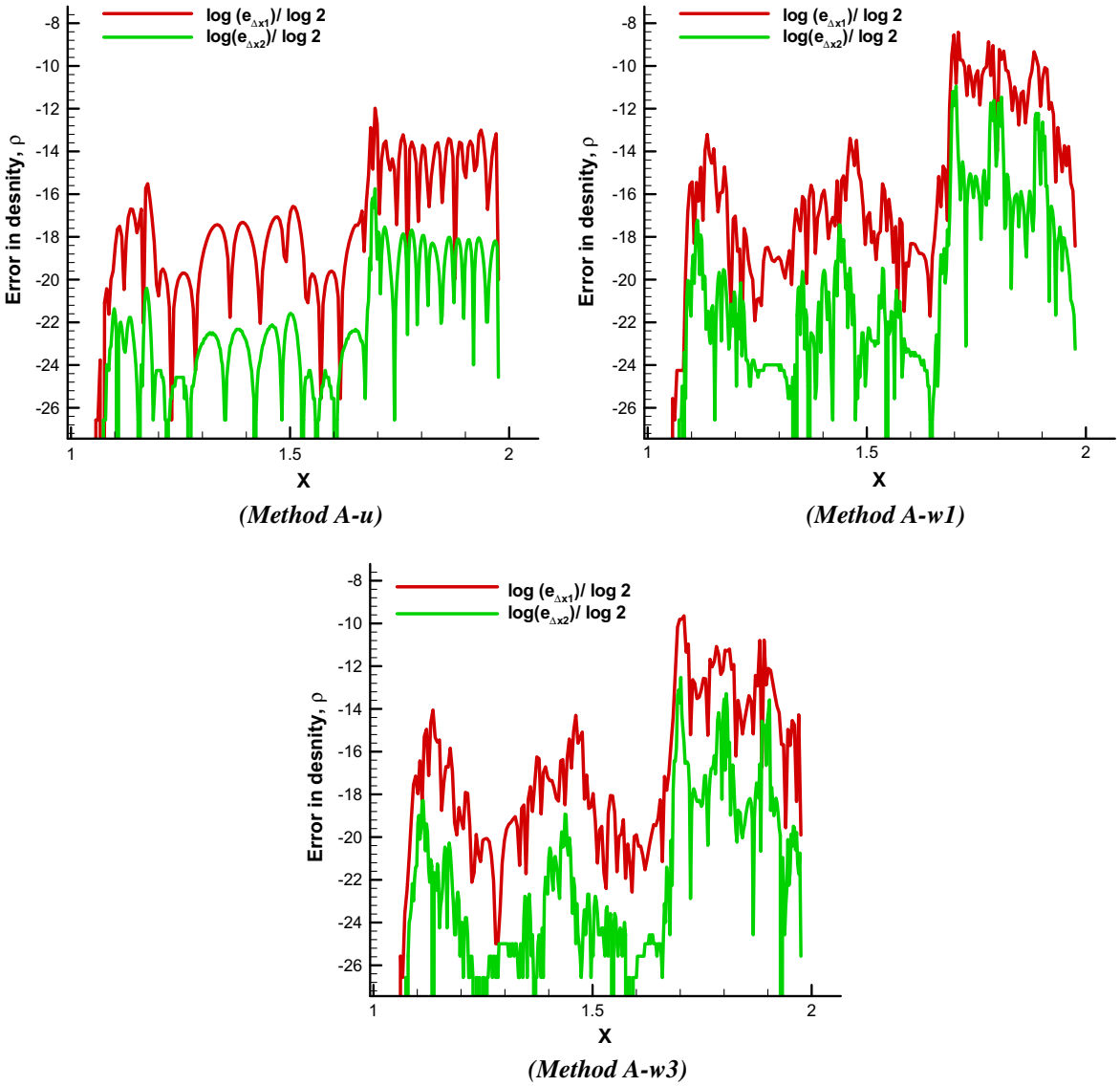

Fig. 14. Comparison of point-wise errors for two sets of grids, $e_{\Delta x1}$ and $e_{\Delta x2}$, in density values computed by three shock-fitting schemes.

used for grid points adjacent to the shock. In general, using one-sided five-point stencils for all three grid points behind the shock (Eq. (49)) gives slightly lesser errors in velocity as compared to those obtained by using Eq. (50). Moreover, velocity values are seen to be converging to the nominal 5th-order accuracy for all four WENO schemes and the upwind difference scheme (Method A-u), even for coarser grids. Errors for methods using the WENO5M scheme (Methods A-w3 and A-w4) are generally three to five times smaller than those obtained with a WENO5 scheme (Methods A-w1 and A-w2).

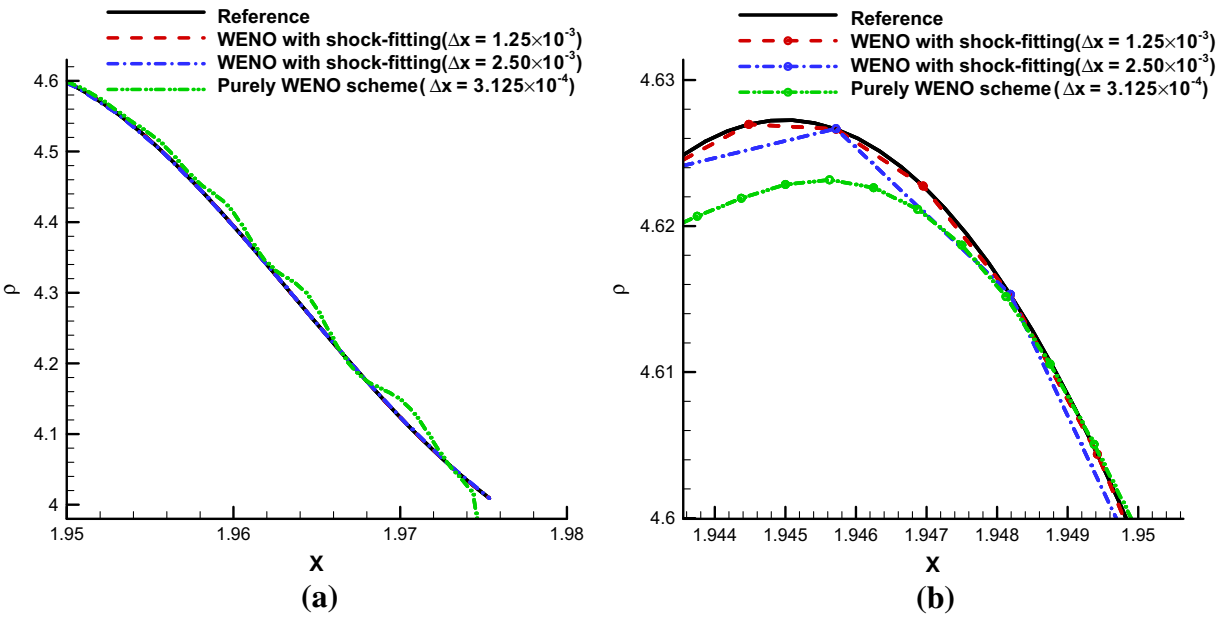

Fig. 15. Comparison of density variation obtained from a shock-fitting scheme with a WENO5 scheme (Method A-w1) and a pure WENO5 scheme: (a) near the shock and (b) away from the shock.

The results computed by using a pure WENO5 shock-capturing scheme are also compared in Tables 5 and 6 with those obtained by the shock-fitting schemes. The results show that the pure 5th-order WENO5 scheme reduces to first-order accuracy for the problem of shock–disturbance interaction because of the discontinuity at the shock. More importantly, the computational errors of the pure WENO5 scheme are about five orders of magnitude larger than those of the conventional shock-fitting scheme (Method A-u), for Grid III. This observation demonstrates the advantage of the shock-fitting approach for the shock–turbulence interaction problems.

Better insight for convergence is obtained by comparing point-wise errors of these methods. Spatial variations of point-wise errors in density values obtained from three shock-fitting methods for Grids I and II are compared in Fig. 14. Since error values are plotted on a log scale with 2 as the base, one can deduce the local order of accuracy, as defined in Eq. (69), by taking the difference between the two profiles in Fig. 14. It can be seen that for all three schemes, errors incurred in the region just behind the shock are higher. This is caused by the fact that local wavelengths of the disturbances immediately behind the shock are much shorter than those away from the shock. As a result, numerical errors are higher there because of a reduction in local grid resolution. For the two shock-fitting methods coupled with the WENO schemes (Methods A-w1 and A-w3), the point-wise errors generally correspond to approximately 4th order accuracy, while the errors for Method A-u with the upwind difference scheme has close to 5th order accuracy. Moreover, errors for Methods A-w1 and A-w3 with the WENO schemes are significantly higher than those for Method A-u with the upwind scheme for the Grids I and II, as shown in the Fig. 14.

Fig. 15 compares the local density profiles obtained from a shock-fitting scheme with a WENO5 scheme (Method A-w1) and a pure WENO5 scheme. Grids I and II are used for Method A-w1 with $\Delta x_1 = 2.5 \times 10^{-3}$ and $\Delta x_2 = 1.25 \times 10^{-3}$. On the other hand, a much finer grid of $\Delta x = 3.125 \times 10^{-4}$ is used for the pure WENO5 scheme because of its larger computational errors. Fig. 15(a) shows that, for this one-dimensional problem of an almost standing shock, post-shock oscillations are observed in the solutions computed by using the pure WENO5 scheme. Such oscillations lead to deterioration of accuracy. From Fig. 15(b), it can be observed that a coarse-grid solution of the shock-fitting scheme is much better than the highly resolved ones obtained by the pure WENO scheme. Hence, it is expected that, for the general shock–disturbance interaction problems, there is a clear advantage of using a shock-fitting algorithm as compared to using a pure shock-capturing scheme.

In summary, the computational results of this section show that shock-fitting algorithms combined with shock-capturing methods are much more accurate than shock-capturing schemes alone for problems of shock disturbance interactions. On the other hand, the accuracy of these combined schemes is slightly poorer than that of Method A-u, which is a shock-fitting method coupled with an upwind finite-difference scheme. Nevertheless, a shock-capturing method coupled with a shock-fitting method should provide more robustness for computing flows where secondary shocks are formed behind the fitted main shock wave.

6. 2-D shock–disturbance interaction computed by a shock-fitting method

Numerical simulation results for two-dimensional disturbances interacting with a shock wave are available in the literature [18,23]. Mahesh [18] carried out both linear-interaction analysis and numerical simulation for a two-dimensional

problem of a normal Mach 1.5 shock interacting with weak plane vorticity-entropy waves traveling at varying angles of incidence. In this paper, the same problem is used to test our 5th-order shock-fitting algorithm of Method A-u. The computational domain is assumed to contain an ideal gas with a specific heat ratio of 1.4. Fluctuations are superposed over a steady Mach 1.5 normal shock solutions (obtained from the Rankine–Hugoniot relations) for the gas. In a shock-fitting setting, disturbances propagate downstream from the inflow boundary and interact with the normal shock as shown in Fig. 16. The interactions of a normal shock and the forcing disturbances cause time-periodic oscillations of the shock front and disturbance amplifications behind the shock.

In shock-fitting Method A-u, a stationary Mach 1.5 shock wave is perturbed at $t = 0$ by imposing a small amplitude disturbance field of the incident plane wave at angle ψ_1 to the x-axis. The incident wave field has the following form:

$$\begin{aligned} u' &= U_1 A_v \sin\psi_1 \cos(k_x x + k_y y - U_1 k_x t) \\ v' &= -U_1 A_v \cos\psi_1 \cos(k_x x + k_y y - U_1 k_x t) \\ \rho' &= \rho_1 A_v \cos\psi_1 \cos(k_x x + k_y y - U_1 k_x t) \\ p' &= 0.0 \end{aligned} \tag{70}$$

where variables U and ρ denote the mean velocity and density, respectively. The variables u', v', p' and ρ' represent fluctuations in velocities, pressure, and density, respectively. Subscripts 1 and 2 denote the upstream and downstream steady states with respect to the shock.

For the computational results presented here, $k_y = k\sin\psi_1 = 1$ and $k_x = k\cos\psi_1$ is used. The domain length in y direction is $L_y = 2\pi$ to ensure that the flow is periodic over the computational domain in the y direction. The flow variables presented here are non-dimensionalized by appropriate combinations of a reference length $L_0 = 2\pi$, a reference pressure p_0^* and a reference density ρ_0^*. Here, p_0^* and ρ_0^* correspond to the unperturbed free-stream values. For the present study, we use $A_v = A_e = 0.025$, i.e., the incoming vorticity and entropy waves in same phase are considered. The shock, represented by the left boundary of the domain, is initially located at $x = 3\pi/2$.

The 2-D problem is computed by solving the Euler equations with our two-dimensional 5th-order shock-fitting algorithm of Method A-u. Periodic boundary conditions are used in the y direction. In streamwise direction x, the shock forms the inflow boundary which is treated by the shock-fitting algorithm. As computations are started, large oscillations in flow properties are observed downstream of the shock. These initial transient solutions propagate downstream followed by an oscillating field. The exit boundary on the right hand side of the computational domain presents a problem for the computations since the flow is subsonic at the exit. Non-reflecting boundary conditions at the exit need to be chosen such that vorticity, acoustic and entropy perturbation in the domain are allowed to propagate out of the domain without spurious reflection. Moreover, we use a sponge layer or buffer zone (Fig. 16) where reflecting waves are damped out. In this paper, we use the non-reflecting boundary conditions of Poinsot and Lele [87] at the outflow boundary and found that vorticity waves leave the domain without reflection. Consequently we are able to obtain time-periodic vorticity solutions downstream of the shock.

Fig. 17 shows the vorticity profile after the initial transients of the solution leave the domain. The shock, which oscillates in response to the forcing waves, is located along the left boundary of the computational domain. It can be seen that a sinusoidal vorticity profile without numerical oscillations is obtained along the x direction.

Mahesh [18] considered linearized Euler equations behind the shock and solved a boundary-value problem for the shock displacement and the flow behind the shock wave. It was found that the solution behind the shock wave has two different

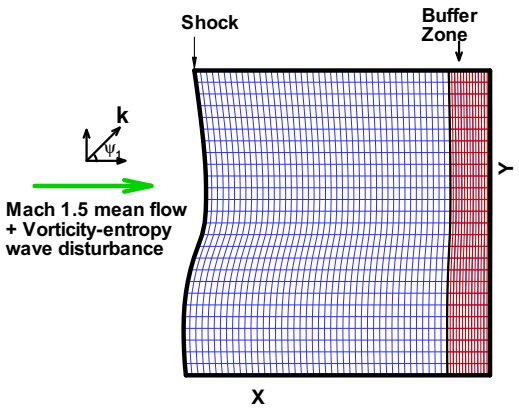

Fig. 16. For the shock and vorticity–entropy wave interaction problem, schematic and computational domain used for a shock-fitting algorithm.

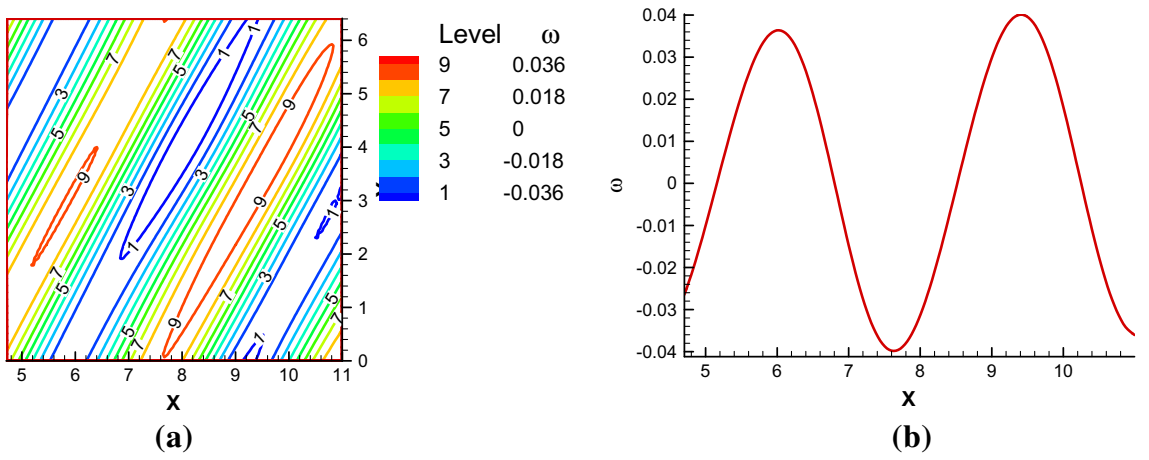

Fig. 17. Interaction of a vorticity–entropy wave for 45° angle of incidence: (a) vorticity contours at t = 15.0 and (b) variation in vorticity values along x-direction at $y = \pi$ (centerline of domain) $t = 15.0$.

regimes that differ in nature of the pressure field. For a given Mach number, the two regimes are demarcated by a critical angle of incidence denoted by ψ_c. If ψ_1 is less than ψ_c, the transmitted pressure field behind the shock is a plane sinusoidal wave. For an incident vorticity or entropy wave, the transmitted waves behind the shock contain all three kinds of waves, i.e., acoustic, vorticity, and entropy waves. However, $\psi_c < \psi_1 < \pi/2$ if, the pressure perturbations behind the shock wave form an evanescent field. There is no transmitted acoustic wave behind the shock, though there are still entropy and vorticity transmitted waves. Linear analysis conducted by Mahesh predicts a value of 61.36° for the critical incidence angle for a Mach 1.5 flow. This information from linear theory was used to qualitatively validate our results.

Fig. 18 shows profiles of instantaneous pressure, vorticity and entropy behind the shock in the x direction along a horizontal line located at $y = \pi$ for three angles of incidence. We define a dimensionless entropy s^* of the fluid at pressure, p and density ρ as follows:

$$s^* = \frac{\ln p}{\gamma} - \ln \rho \tag{71}$$

It can be seen from this figure that the pressure profiles are sinusoidal for the cases of $\psi_1 = 15°$ and $\psi_1 = 45°$, where ψ_1 is less than ψ_c. In addition, the wavelength for oscillations in the x direction increases significantly when ψ_1 increases from 15° to 45°. This is in agreement with the linear theory that the wavenumber in the x direction is proportional to $\cos\psi_1$ for a fixed Mach number of the incoming flow. In addition, for the case of $\psi_1 = 75° > \psi_c$, as expected, the computed pressure profiles approach an asymptotic constant value of the steady state solution behind the shock. In this case, pressure perturbations decrease exponentially as we move downstream behind the shock. Fig. 18 also shows that the profiles of both vorticity and entropy are sinusoidal variations for all three incident angles. Similar to the pressure waves, the wavelength along the x direction increases with the increasing incidence wave angle. While the pressure perturbations show different behaviors in the two regimes, the transmitted vorticity and entropy waves remain sinusoidal for any incident angle. This behavior is predicted by the linear theory and thus qualitatively confirms the validity of the results obtained from the current shock-fitting computations.

The linear theory reported by Mahesh [18] provides amplification factors for perturbations in vorticities, $\overline{\omega_2'^2}/\overline{\omega_1'^2}$. As shown in Fig. 18, vorticity perturbations downstream of the shock are plane waves for all angles of incidence. After the initial transient solutions leave the computational domain, statistics of the vorticity perturbations are calculated over a period of time for the inflow disturbance ($2\pi/U_1 k_x$). Fig. 19 compares the amplification factors, $\overline{\omega_2'^2}/\overline{\omega_1'^2}$, obtained from our shock-fitting solutions to the numerical and theoretical solutions published by Mahesh. Our shock-fitting results have a very good agreement with those of the linear theory solutions. It is noticed that Mahesh's results do not agree with the linear theory results when the incident angle is 61.36°, which is equal to the critical value of ψ_c. On the other hand, the results of the shock-fitting method (Method A-u) agree well with those of the linear theory.

Overall, for the test case of two-dimensional shock–disturbance interaction, the results of conventional shock-fitting method are in a good agreement with those of the linear theory. It is important to note that, for the same problem, standard shock-capturing schemes suffer from spurious numerical oscillations for the cases when the incidence angle of disturbance waves is equal or greater than the critical angle ψ_c. Fig. 20 compares density distributions obtained from the pure WENO5 scheme and those computed by two shock-fitting schemes: Method A-u and Method A-w1. The incident angle is 75°, which is larger than the critical angle. For a good comparison of the pure WENO5 results with those obtained from the shock-fitting schemes, we use two computational domains on both sides of the fitted shock and results. It is observed that, at this incident angle, the shock-capturing scheme produces spurious oscillations in the wave field

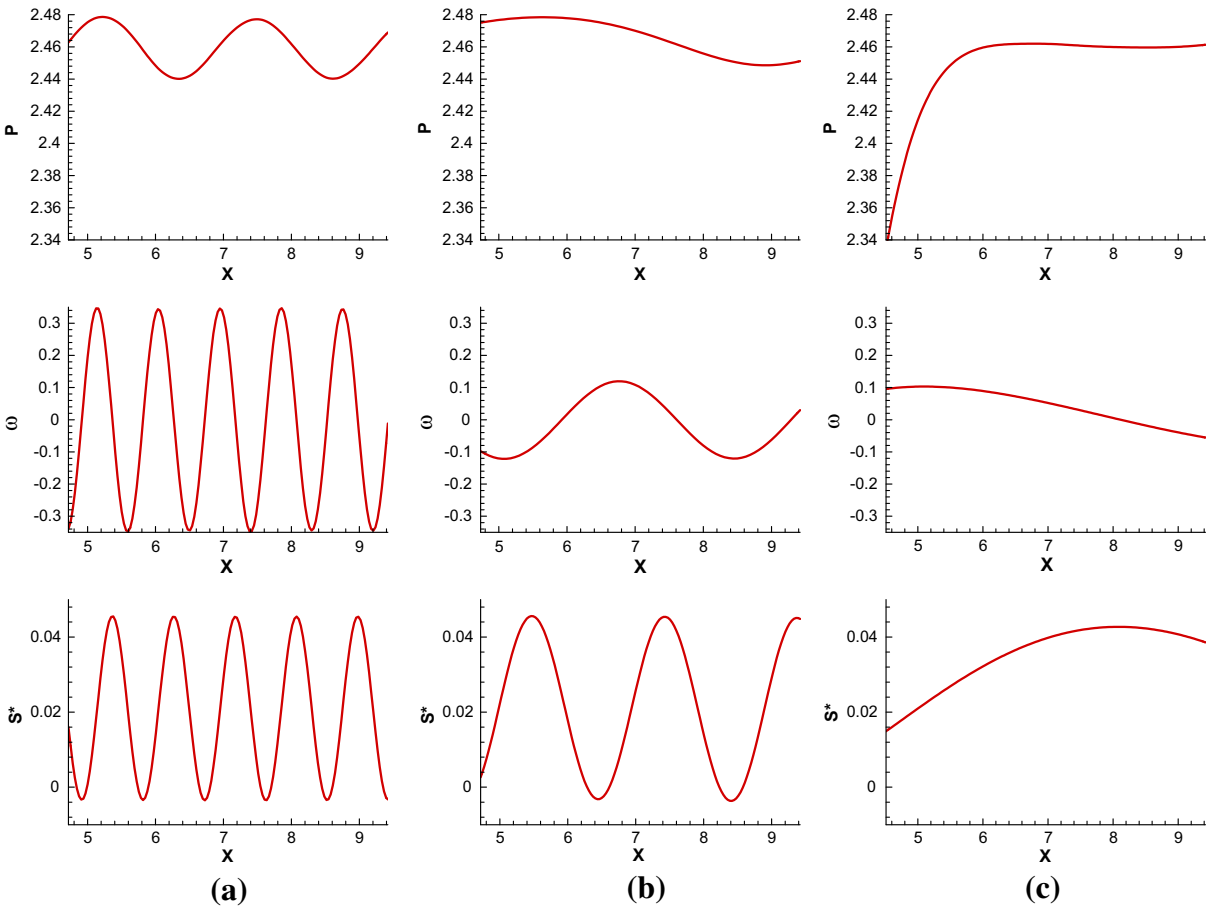

Fig. 18. Profiles of instantaneous pressure, vorticity, and entropy distributions in the x direction along $y = \pi$ for disturbances coming at three angles of incidence at $t = 10$: (a) $\psi_1 = 15°$, (b) $\psi_1 = 45°$, and (c) $\psi_1 = 75°$.

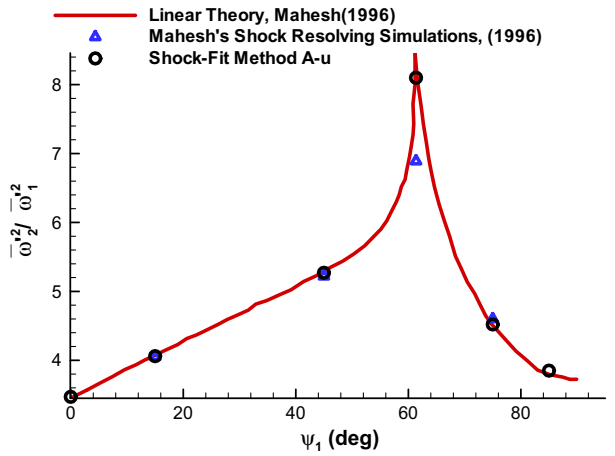

Fig. 19. Comparison of amplifications in vorticity fluctuations, $\overline{\omega_2'^2}/\overline{\omega_1'^2}$, as obtained from three different methods: current shock-fitting scheme (Method A-u), the linear theory and simulation results of Mahesh [18].

behind the shock. Such spurious oscillations do not exist in both shock-fitting solutions. Thus, Fig. 20 demonstrates that the shock-fitting is superior for the problem of shock–turbulence interaction if the main shock maintains a well-defined front.

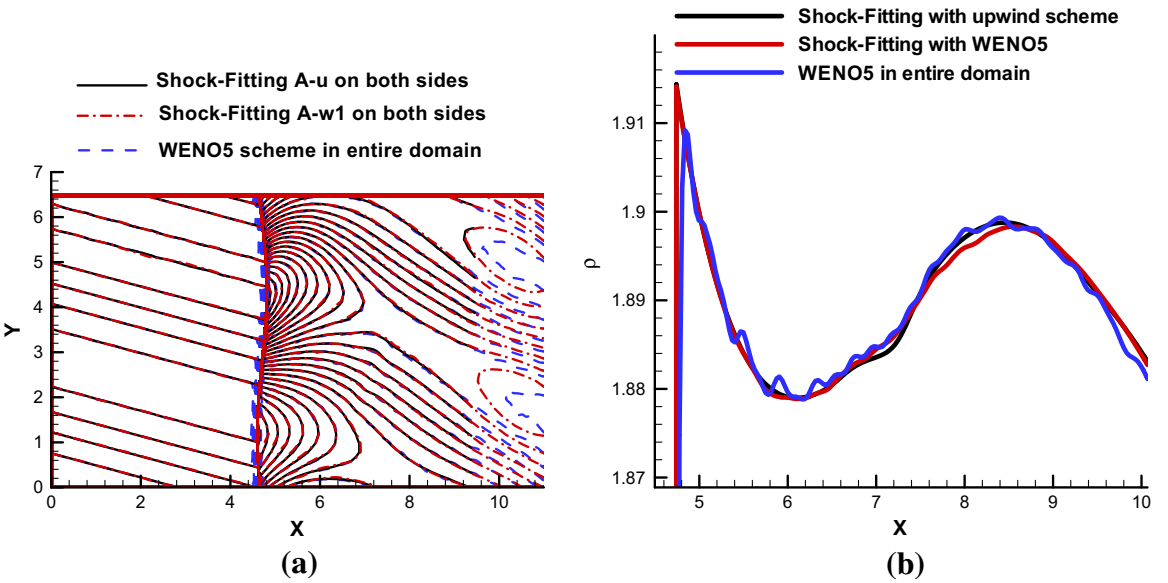

Fig. 20. Comparison of density distributions obtained from three schemes, the pure WENO5 scheme, and two shock-fitting schemes of Method A-u and Method A-w1: (a) instantaneous contours at $t = 10$, and (b) profiles along $y = \pi$ line.

7. Results of fixed-grid shock-fitting schemes

The 1-D and 2-D flow problems considered in the previous sections are used in this section to test our new two-dimensional front-tracking (fixed-grid) shock-fitting algorithm described in Section 4. In a fixed-grid setting, the governing flow equations are solved both ahead of the shock and behind the shock. A schematic of the computational set-up is shown in Fig. 21. The shock front is represented by an array of marker points which are defined as the intersections of shock-front with the grid lines. The grid lines are fixed and the shock can freely move over the underlying grid points. As a benchmark for validation of front-tracking shock-fitting schemes, we use the conventional shock-fitting algorithm, Method A-u, to solve the flow fields on both sides of the shock. The computational domain of this implementation of the shock-fitting scheme is showed in Fig. 21(b). Both sides of shock are treated as separate zones with the shock as common boundary. Since the flow behind the shock is subsonic, we use non-reflecting boundary conditions with a buffer zone. Periodic boundary conditions were used in the y direction.

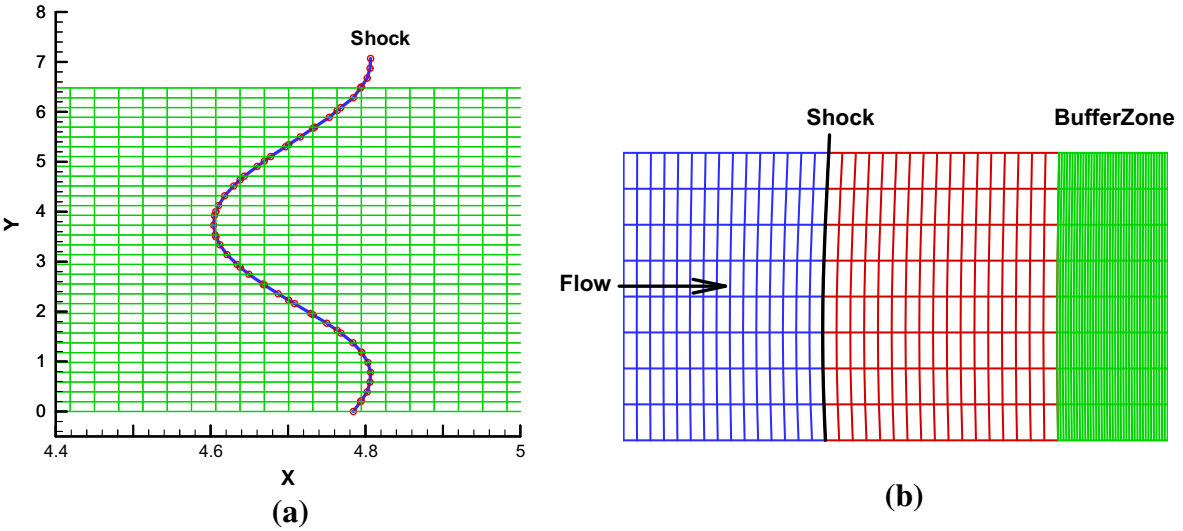

Fig. 21. Schematics of computational set-ups for the shock–disturbance interaction problem: (a) a part of the computational domain for a fixed-grid front-tracking based shock-fitting scheme and (b) computational domain for multi-zone moving grid shock-fitting method.

7.1. Order of accuracy evaluation of fixed-grid shock-fitting methods

To test the order of accuracy of the solution with the front-tracking method, we carry out the grid-convergence study similar to that presented in Section 5 for the moving-grid shock-fitting schemes. The same shock–disturbance interaction problem described in Section 5.1 is used to test the fixed-grid shock-fitting scheme.

For the conventional moving-grid shock-fitting methods in Section 5, the reference frame is fixed with the mean shock motion so that the shock is stationary when the disturbances are absent. For the fixed-grid shock-fitting computations, shock waves can move freely across the grid lines. To test the capability of this property of the method, the reference frame is set such that a Mach 3 shock moves into still fluid with density variations. Thus flow conditions upstream of the moving shock are

$$\begin{aligned} \rho &= 1.0 + \varepsilon \sin^4(2.5\pi x) \\ u &= 0.0 \\ p &= 1.0 \end{aligned} \tag{72}$$

Fig. 22 shows density profiles and errors at the final time of $t = 0.32$ for the shock–disturbance interaction problem computed by the fixed-grid shock-fitting scheme for Grids I and II. In the density distributions shown in Fig. 22(a), the solutions of these grids are indistinguishable from the reference solution in the figure. The spatial variations of point-wise errors for Grids I and II are compared in Fig. 22(b). It can be observed that the errors for the finer grid are significantly smaller than those of the coarser grid. As defined in Eq. (69), the differences between the two lines in Fig. 22(b) represents the computational order of accuracy of the method. It can be seen in the figure that the current fixed-grid shock-fitting scheme is approximately 5th order accurate at almost all spatial points.

To quantify the computational order of accuracy of the method, we take the L-1 norm of local errors and compute the approximate error of convergence from Eq. (69) for different sets of grids. These values are tabulated in Table 7. It is found that the fixed-grid shock-fitting method has a convergence rate close to the 5th order for flow variables. The method is 4th-order accurate for the shock locations. These results are expected from our method which uses a 5th-order upwind scheme

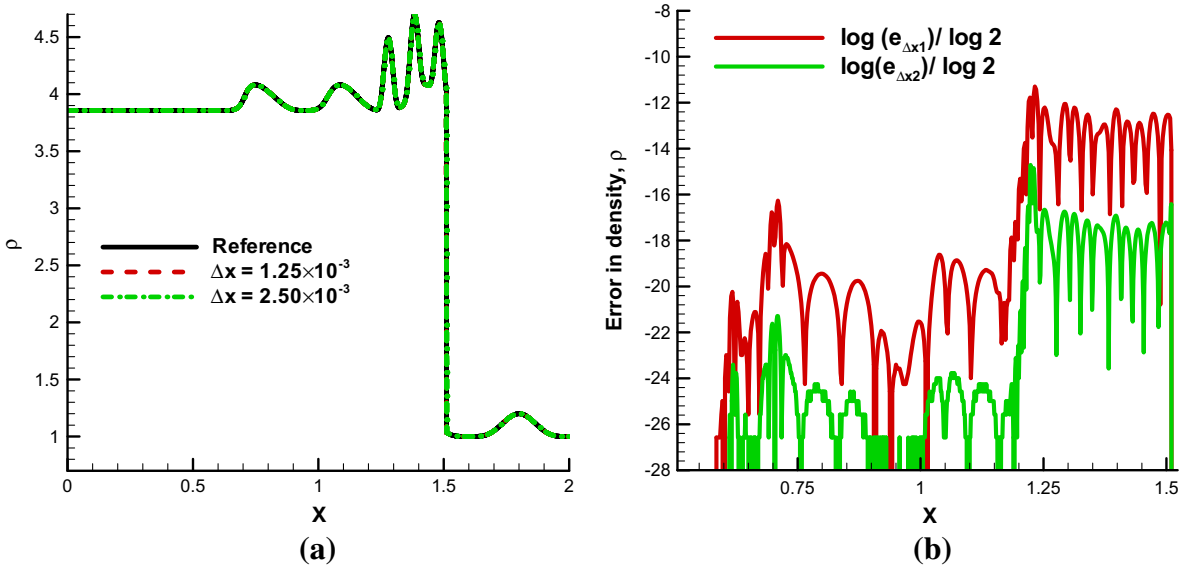

Fig. 22. (a) Instantaneous density variation at $t = 0.32$ for the shock–disturbance interaction problem computed by the fixed-grid shock-fitting scheme for three different grids and (b) point-wise errors for two sets of the grids, $e_{\Delta x1}$ and $e_{\Delta x2}$.

Table 7
L-1 errors and grid convergence of fixed grid shock-fitting.

	Error I: $e_{\Delta x_1}$	Error II: $e_{\Delta x_2}$	Error III: $e_{\Delta x_3}$	Order from I and II	Order from II and III
Density	3.48E−05	1.73E−06	9.16E−08	4.34	4.24
Velocity	5.55E−07	1.81E−08	5.77E−10	4.94	4.97
Pressure	4.29E−06	1.43E−07	4.68E−09	4.91	4.93
Shock-location	2.81E−08	7.48E−10	4.48E−11	5.23	4.07

in the interior with a 4th-order one-sided finite-difference algorithm near the shock. Moreover, the results show that the new fixed-grid shock-fitting solution does not incur spurious oscillations around the shock. This provides evidence of the advantages of using shock-fitting methods for the shock–turbulence interaction problems.

7.2. Results for 2-D shock and disturbance interaction

In this section, the new fixed-grid shock-fitting method is tested in the same 2-D shock–disturbance interaction problem described in Section 6. Several cases of different incident wave angles are computed. The results are compared with those obtained by the conventional moving-grid shock-fitting scheme (Method A-u).

Fig. 23 shows instantaneous solutions for the interaction of a vorticity-entropy wave with a shock with at an incidence angle of $\psi_1 = 15^\circ$ at $t = 10.0$. It can be seen that a sinusoidal density profile is obtained along the x-direction. Again, no spurious numerical oscillations are observed in the shock-fitting solutions. The figure also shows the unsteady shock front obtained by the method. The shock interface itself is sinusoidal as expected from linear theory.

As a benchmark for validation of the front-tracking results, we use the conventional shock-fitting algorithm of Method A-u for comparison. Both sides of the shock are treated as separate zones, with the shock as a common boundary. A fifth-order

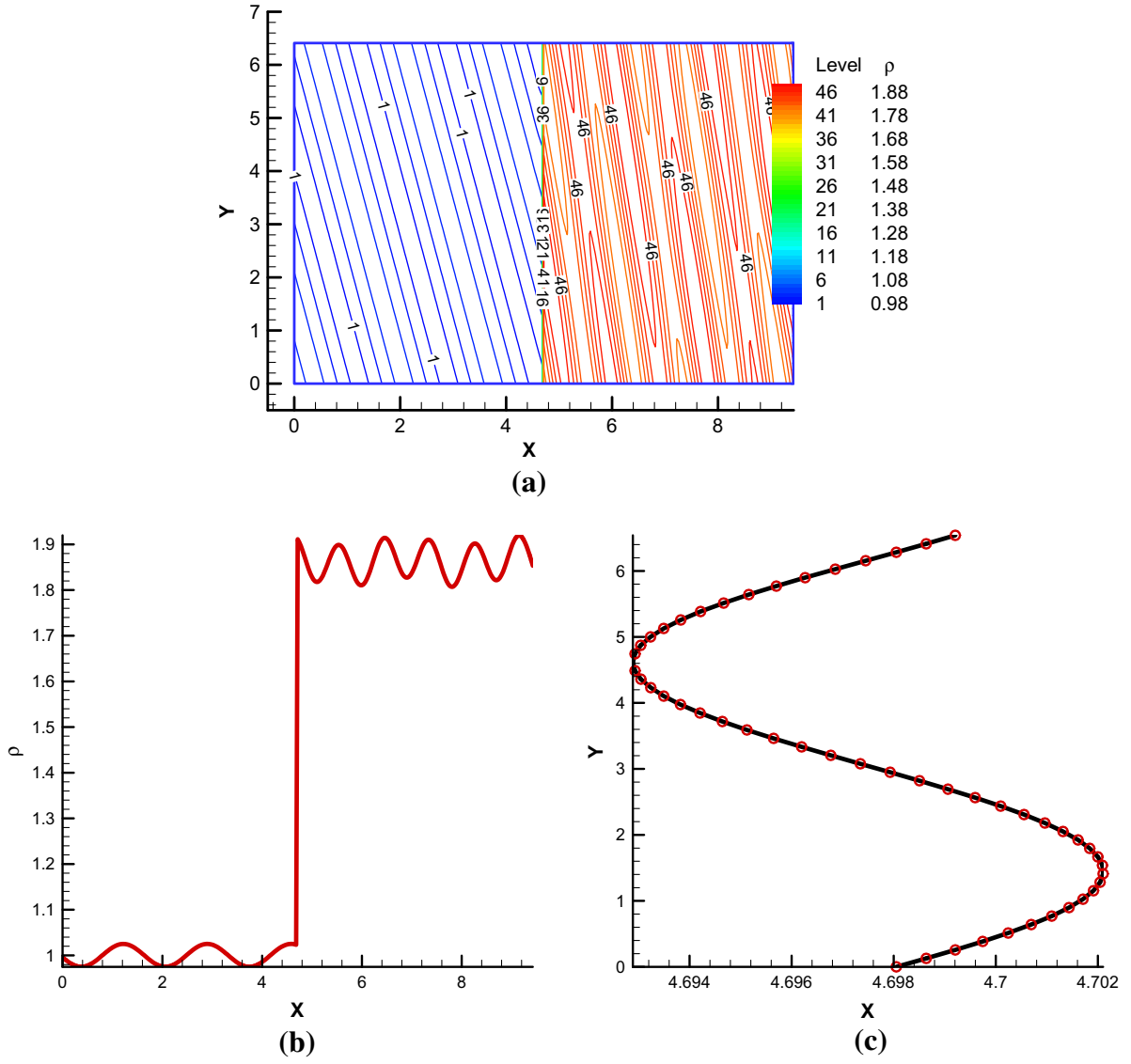

Fig. 23. Instantaneous solutions for the interaction of a vorticity–entropy wave with a shock with $\psi_1 = 15^\circ$ at $t = 10.0$: (a) contours of density, (b) density distribution along the center line of the domain at $y = \pi$, and (c) shock front defined by marker points.

upwind finite-difference scheme is applied separately on both sides of the shock. Fig. 24 compares the results of the current front-tracking shock-fitting method and the moving-grid shock-fitting method for the case of 45° angle of incidence at $t = 10$. We see that the front-tracking results agree very well with those obtained from the conventional shock-fitting method on moving-grids for all the variables. Since the incidence angle ψ_1 is less than ψ_c in this case, the transmitted waves for pressure, vorticity, and entropy remain sinusoidal behind the shock. Fig. 24 also compares the shock fronts captured by the two versions of the shock-fitting methods. Fig. 24(d) shows that the shock profile is sinusoidal and the shock moves through the underlying fixed grid. In addition, the location and shock shape computed by using the front-tracking method agrees very well to those obtained by Method A-u of the conventional moving-grid shock-fitting method.

Fig. 25 compares the results of the two shock-fitting schemes for the case of $\psi_1 = 75°$. The incidence angle of this case is larger than the critical value ψ_c. Again, the variations in flow variables obtained by the front-tracking method agree very well with those obtained from Method A-u. As compared to the results for the case of 45° angle of incidence, the transmitted entropy wave and vorticity wave have larger wavelengths while they still remain sinusoidal as expected. The pressure fluctu-

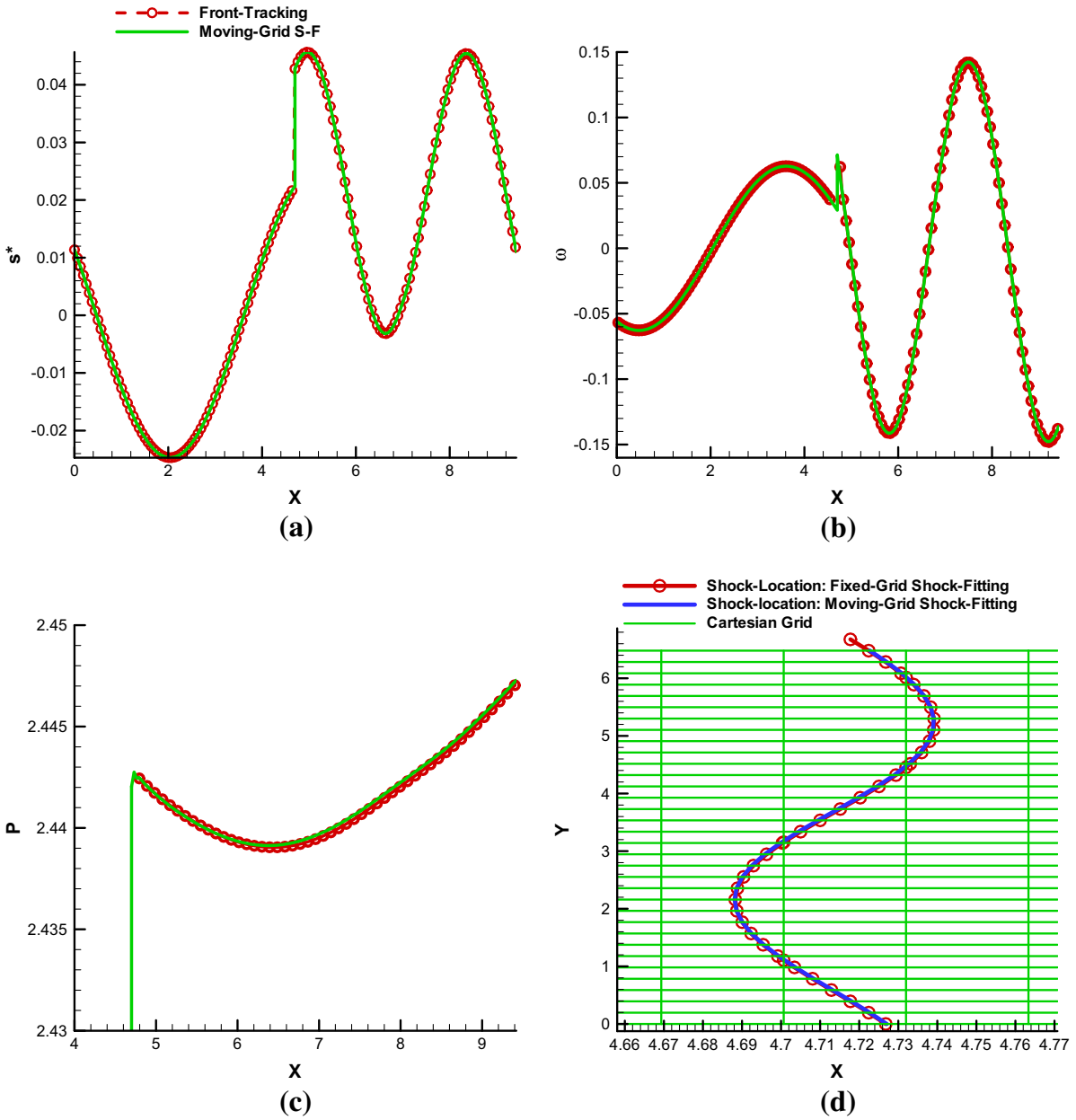

Fig. 24. Comparison of instantaneous flow variables and shock front computed from the conventional shock-fitting Method A-u and the new fixed-grid shock-fitting method for distributions along the center line at $y = \pi$ at $t = 10$. The case has a 45° angle of incidence.

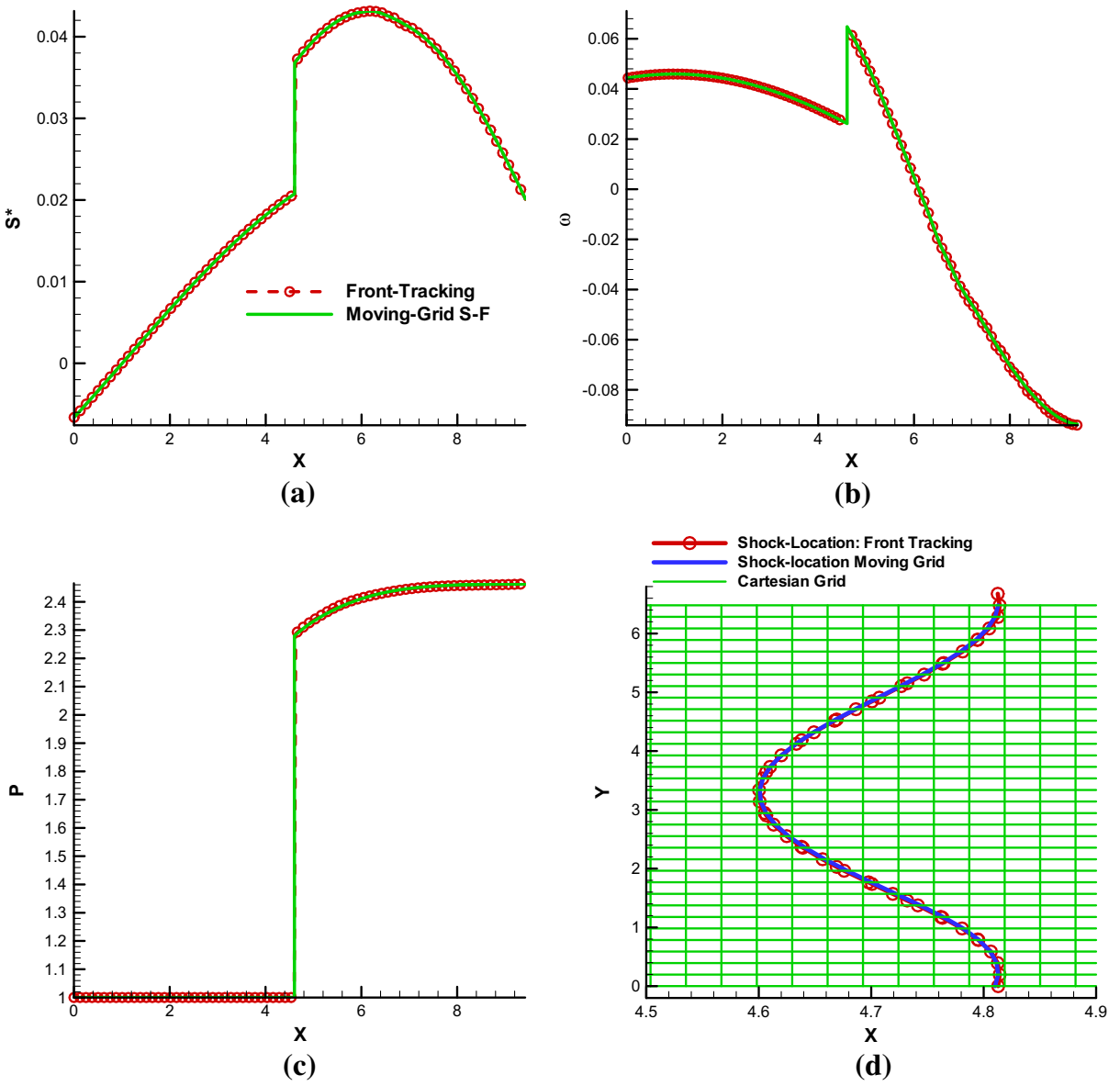

Fig. 25. Comparison of instantaneous flow variables and shock front computed from the conventional shock-fitting method (Method A-u) and the new fixed-grid shock-fitting method for distributions along the center line at $y = \pi$ at $t = 10$. The case has a 75° angle of incidence.

ations, however, are an evanescent field as predicted by linear theory. Similarly, the interface data presented in this figure shows that the front-tracking method predicts the location and geometry of the shock well.

In summary, our test results show that the new fixed-grid (front-tracking) shock-fitting method maintains high-order accuracy for computing the shock–disturbance interaction problem. The new method also compares very well with the conventional shock-fitting method, i.e., Method A-u for the 2-D shock–disturbance interaction problem. Although the results obtained from the 2-D front-tracking method are found to be satisfactory for the problem considered here, the algorithm still needs further improvement. For example, the front-tracking algorithm was found to be very tedious to implement when a high-order approximation is required. High-order implementation may be more prone to spurious numerical oscillations when points need to be removed in the grid stencils. Moreover, it is found in the numerical computations that as the amplitudes of the incoming waves are increased, the conventional moving-grid shock-fitting methods are much more robust as compared to the front-tracking shock-fitting method. Therefore, for a shock–turbulence interaction problem with a relatively simple shock front, the conventional moving-grid shock-fitting methods in a multi-zone setting are more suitable than the current implementation of front-tracking shock-fitting method. Nevertheless, the results presented here offer ample motivation for developing the fixed-grid shock-fitting as a uniformly high order alternative for problems with more complex shock geometry.

8. Conclusions

We have developed a new high-order front-tracking shock-fitting method for the shock–turbulence interaction problems, and have carried out grid-convergence analysis for different variations of shock-fitting methods with both moving and fixed grids. We find that fifth-order accuracy is obtained when the conventional shock acceleration based method is used for computing the shock velocities. This is the case when either the fifth-order upwind scheme or fifth-order WENO schemes are used for discretizing the spatial derivatives in the flow equations. However, our results show that other methods for computing shock advancement lead to deterioration in computational accuracy. For the two-dimensional shock–disturbance interaction problem, computational results from the conventional 5th-order shock-fitting algorithm agree very well with the predictions of a linear-interaction analysis. We have also tested the new front-tracking implementation of the shock-fitting scheme on a fixed grid. Our test results show that the new fixed-grid (front-tracking) shock-fitting method maintains high-order accuracy for computing the shock–disturbance interaction problem. The new method also compares very well with the conventional shock-fitting method for the 2-D shock–disturbance interaction problem. It is also shown that a pure high-order shock-capturing scheme suffers from a reduction in accuracy and spurious numerical oscillations for such problems. Thus shock-fitting methodology offers a high-order alternative for problems involving shock–turbulence interaction.

Acknowledgments

This research is supported by US Department of Energy under Contract No. "DE-FC02-06ER25797:A002" as part of a SciDAC (Scientific Discovery through Advanced Computing) project with "Science Application" in Turbulence with Dr. Lali Chatterjee as program manager. The authors would like to thank Prof. S.K. Lele, Prof. P. Moin and Dr. J. Larsson of the Stanford University; Drs. A. Cook, W. Cabot, B. Sjögreen of the Lawrence Livermore National Laboratory and Dr. H.C. Yee of the NASA Ames Research Center for their valuable suggestions during the course of this work.

References

[1] S. Lee, S.K. Lele, P. Moin, Interaction of isotropic turbulence with shock waves: effect of shock strength, Journal of Fluid Mechanics 340 (1997) 225–247.
[2] K.A. Mahesh, L. Lee, S.K. Lele, P. Moin, The interaction of an isotropic field of acoustic waves with a shock wave, Journal of Fluid Mechanics 300 (1995) 383–407.
[3] K.A. Mahesh, S.K. Lele, P. Moin, The influence of entropy fluctuations on the interaction of turbulence with a shock wave, Journal of Fluid Mechanics 334 (1997) 353–379.
[4] S. Jamme, J.B. Cazalbou, F. Torres, P. Chassaing, Direct numerical simulation of the interaction between a shock wave and various types of isotropic turbulence, Flow, Turbulence and Combustion 68 (2002) 227–268.
[5] T.K. Lee, X. Zhong, Spurious numerical oscillations in simulation of supersonic flows using shock-capturing schemes, AIAA Journal 37 (3) (1999) 313–319.
[6] L.S.G. Kovasznay, Turbulence in supersonic flow, Journal of the Aeronautical Sciences 20 (10) (1953) 657–682.
[7] B.T. Chu, L.S.G. Kovasznay, Nonlinear interactions in a viscous heat-conducting compressible gas, Journal of Fluid Mechanics 3 (1958) 494–514.
[8] H.S. Ribner, Convection of a Pattern of Vorticity through a Shock Wave, NACA TN-2864 (also as NACA Report 1164 1953), 1953.
[9] H.S. Ribner, Shock–turbulence Interaction and the Generation of Noise, NACA TN-3255 (also as NACA Report 1233), 1954.
[10] H.S. Ribner, Acoustic energy flux from shock–turbulence interaction, Journal of Fluid Mechanics 35 (1969) 299–310.
[11] F.K. Moore, Unsteady Oblique Interaction of a Shock Wave with a Plane Disturbances, NACA TN-2879 (Also as NACA Rep. 1165), 1953.
[12] J.L. Kerrebrock, The Interaction of Flow Discontinuities with Small Disturbances in a Compressible Fluid, Ph.D. Thesis, California Institute of Technology, 1956.
[13] J.F. McKenzie, K.O. Westphal, Interaction of linear waves with oblique shock waves, Physics of Fluids 11 (1968) 2350–2362.
[14] M.E. Goldstein, Turbulence generated by the interaction of entropy fluctuations with non-uniform mean flows, Journal of Fluid Mechanics 93 (1979) 209–224.
[15] L. Lee, P. Moin, S.K. Lele, Interaction of isotropic turbulence with a shock wave, Report TF-52. Dept. Mech. Eng., Stanford Univ., CA, 1992.
[16] L. Lee, S.K. Lele, P. Moin, Direct numerical simulation of isotropic turbulence interacting with a weak shock wave, Journal of Fluid Mechanics 251 (1993) 533–562.
[17] L. Lee, S.K. Lele, P. Moin, Interaction of Isotropic Turbulence with a Strong Shock Wave, AIAA Paper 94-0311, 1994.
[18] K.A. Mahesh, P. Moin, S.K. Lele, The Interaction of a Shock Wave with a Turbulent Shear Flow, Report TF-69, Thermosciences Division, Mechanical Engineering Department, Stanford University, 1996.
[19] D. Fabre, L. Jacquin, J. Sesterhenn, Linear interaction of a cylindrical entropy spot with a shock, Journal of Physics of Fluids A 13 (8) (2001) 2403–2422.
[20] S.P. Pao, M.D. Salas, A Numerical Study of Two-dimensional Shock Vortex Interaction, AIAA Paper 81-1205, 1981.
[21] M.Y. Hussaini, D. Kopriva, M.D. Salas, T.A. Zang, Spectral methods for the Euler equations. II – Chebyshev methods and shock fitting, AIAA Journal 23 (1987) 234–240.
[22] K.R. Meadows, A. Kumar, M.Y. Hussaini, Computational study on the interaction between a vortex and a shock wave, AIAA Journal 29 (2) (1991) 174–179.
[23] T.A. Zang, M.Y. Hussaini, D.M. Bushnell, Numerical computations of turbulence amplification in shock-wave interactions, AIAA Journal 22 (1) (1984) 13–21.
[24] K.R. Meadows, J. Casper, Computing unsteady shock waves for aeroacoustic applications, AIAA Paper (1993) 1993–4329.
[25] F. Grasso, S. Pirozzoli, Shock-wave–vortex interactions: shock and vortex deformations, and sound production, Theoretical and Computational Fluid Dynamics 13 (6) (1993) 421–456.
[26] Y. Andreopoulos, J.H. Agui, G. Briassulis, Shock wave–turbulence interactions, Annual Review of Fluid Mechanics 32 (2000) 309–345.
[27] R. Hannappel, R. Friedrich, Direct numerical simulation of a Mach 2 shock interacting with isotropic turbulence, Applied Scientific Research 54 (1995) 205–221.
[28] S. Jamme, J.B. Cazalbou, F. Torres, P. Chassaing, Direct numerical simulation of the interaction between a shock wave and various types of isotropic turbulence, Turbulence and Combustion 68 (2002) 227–268.
[29] N.A. Adams, K. Shariff, A high-resolution hybrid compact-ENO scheme for shock turbulence interaction problems, Journal of Computational Physics 127 (27) (1996) 57.

[30] N.A. Adams, K. Shariff, Direct numerical simulation of turbulent compression corner flow, Theoretical and Computational Fluid Dynamics 12 (1998) 109–129.
[31] S. Pirozzoli, Conservative hybrid compact-WENO schemes for shock–turbulence interaction, Journal of Computational Physics 178 (1) (2002) 81–117.
[32] F. Ducros, V. Ferrand, F. Nicoud, C. Weber, D. Darracq, C. Gacherieu, T. Poinsot, Large eddy simulation of the shock/turbulence interaction, Journal of Computational Physics 152 (1999) 517–549.
[33] H.C. Yee, N.D. Sandham, M.J. Djomehri, Low dissipative high-order shock capturing methods using characteristic based filters, Journal of Computational Physics 150 (1999) 199–238.
[34] B. Sjogreen, H.C. Yee, Multiresolution wavelet based adaptive numerical dissipation control for high order methods, Journal of Scientific Computing 20 (2) (2004) 211–215.
[35] A.W. Cook, W.H. Cabot, M.L. Welcone, P.L. Williams, B.J. Miller, B.R. de Supinski, R.K. Yates, Tera-scalable Algorithms for Variable-density Elliptic Hydrodynamics with Spectral Accuracy, LLNL Report No. UCRL-CONF-211384, 2005.
[36] J. Sesterhenn, Direct numerical simulation of the interaction of isotropic turbulence with a shock wave using shock-fitting, Comptes rendus. Mecanique [1631-0721] 333 (1) (2005) 87–93.
[37] G. Moretti, M. Abbett, A time-dependent computational method for blunt body flows, AIAA Journal 4 (1966) 2136–2141.
[38] G. Moretti, G. Bleich, Three-dimensional flow around blunt bodies, AIAA Journal 5 (1967) 1558–1562.
[39] G. Moretti, Three-dimensional supersonic flow computations, AIAA Journal 1 (1963) 2192–2193.
[40] G. Moretti, Inviscid flowfield about a pointed cone at an angle of attack, AIAA Journal 5 (1967) 789–791.
[41] C.P. Kentzer, Discretization of boundary conditions on moving discontinuities, Lecture Notes in Physics 8 (1970) 108–113.
[42] T. de Neef, G. Moretti, Shock fitting for everybody, Computers and Fluids 8 (1980) 327–334.
[43] G. Moretti, The lambda-scheme, Computers and Fluids 7 (1979) 191–205.
[44] G. Moretti, M.T. di Piano, An Improved Lambda-scheme for One-Dimensional Flows, NASA CR 3712,vol. 15, 1983.
[45] M. Valorani, B. Favini, On the numerical integration of multidimensional initial boundary value problems for the Euler equations in quasi-linear form, Numerical Methods for Partial Differential Equations 14 (1983) 781–814.
[46] L. Zannetti, G. Moretti, Numerical experiments on the leading edge flow field, AIAA Journal 20 (1982) 1668–1673.
[47] A. Dadone, G. Moretti, Fast Euler solver for transonic airfoils, AIAA Journal 26 (1988) 409–416.
[48] G. Moretti, A technique for integrating two-dimensional Euler equations, Computers and Fluids 15 (1988) 59–75.
[49] G. Moretti, Experiments in Multi-dimensional Floating Shock Fitting, Polytechnic Institute of Brooklyn, 1973.PIBAL Rept. 73-18, August 1973.
[50] M.D. Salas, Shock-fitting method for complicated two-dimensional supersonic flows, AIAA Journal 14 (5) (1976) 583–588.
[51] G. Moretti, A technique for integrating two-dimensional Euler equations, Computers and Fluids 15 (1987) 59–75.
[52] G. Moretti, Computations of flows with shock, Annual Review of Fluid Mechanics 19 (1987) 313–337.
[53] G. Moretti, Thirty-six years of shock fitting, Computers and Fluids 31 (4–7) (2002) 719–723.
[54] D.A. Kopriva, A multidomain spectral collocation computation of the sound generated by a shock–vortex interaction, in: D. Lee, M.H. Schultz (Eds.), Computational Acoustics: Algorithms and Applications, vol. 2, Elsevier Science Publishers, Amsterdam, Netherlands, 1998.
[55] D.A. Kopriva, T. Zang, M.Y. Hussaini, Spectral methods for the Euler equations – the blunt body problem revisited, AIAA Journal 29 (9) (1991) 1458–1462.
[56] D.A. Kopriva, Shock-fitted multidomain solution of supersonic flows, Computer Methods in Applied Mechanics and Engineering 175 (3–4) (1999) 383–394.
[57] W. Cai, High-order hybrid numerical simulations of two-dimensional detonation waves, AIAA Journal 34 (7) (1995) 1248–1255.
[58] X. Zhong, High-order finite-difference schemes for numerical simulation of hypersonic boundary-layer transition, Journal of Computational Physics 144 (1998) 662–709.
[59] Y. Ma, X. Zhong, Receptivity of a supersonic boundary layer over a flat plate. Part 1: Wave structures and interactions, Journal of Fluid Mechanics 488 (2003) 31–78.
[60] Y. Ma, X. Zhong, Receptivity of a supersonic boundary layer over a flat plate. Part 2: Receptivity to freestream sound, Journal of Fluid Mechanics 488 (2003) 79–121.
[61] Y. Ma, X. Zhong, Receptivity to freestream disturbances of Mach 8 flow over a sharp wedge, in: 41st AIAA Fluid Dynamics Conference and Exhibit, AIAA Paper 2003-0788, 2003.
[62] X. Zhong, Leading-edge receptivity to free stream disturbance waves for hypersonic flow over a parabola, Journal of Fluid Mechanics 441 (2001) 315–367.
[63] Y. Ma, X. Zhong, Receptivity of a supersonic boundary layer over a flat plate. Part 3: Effects of different types of free-stream disturbances, Journal of Fluid Mechanics 532 (2005) 63–109.
[64] G.P. Brooks, J.M. Powers, Standardized pseudospectral formulation of the inviscid supsersonic blunt body problem, Journal of Computational Physics 197 (1) (2004) 58–85.
[65] S. Mahlmann, W. Schroder, Disturbance evolution in the leading-edge region of a blunt flat plate in supersonic flow, Fluid Dynamics Research 40 (2008) 803–826.
[66] M.H. Carpenter, J.H. Casper, Accuracy of shock capturing in two spatial dimensions, AIAA Journal 37 (9) (1999) 1072–1079.
[67] X. Zhong, Y. Ma, Boundary-layer receptivity of Mach 7.99 flow over a blunt cone to free-stream acoustic waves, Journal of Fluid Mechanics 556 (2005) 55–103.
[68] A.K. Henrick, T.D. Aslam, J.M. Powers, Simulations of pulsating one-dimensional detonations with true fifth order accuracy, Journal of Computational Physics 213 (1) (2005) 311–329.
[69] G.S. Jiang, C.W. Shu, Efficient implementation of weighted ENO schemes, Journal of Computational Physics 126 (1) (1996) 202–228.
[70] P. Moin, K. Mahesh, Direct numerical simulation: a tool in turbulence research, Annual Review of Fluid Mechanics 30 (1998) 539–578.
[71] P.L. Roe, Approximate Riemann solvers, parameter vectors, and difference schemes, Journal of Computational Physics 43 (2) (1981) 357–372.
[72] C. Peskin, The immersed boundary method, Acta Numerica (2002) 479–527.
[73] X. Zhong, A new high-order immersed interface method for solving elliptic equations with imbedded interface of discontinuity, Journal of Computational Physics 225 (1) (2007) 1066–1099.
[74] R.P. Fedkiw, T.D. Aslam, S. Xu, The ghost fluid method for deflagration and detonation discontinuities, Journal of Computational Physics 154 (2) (1999) 393–427.
[75] S.A. Unverdi, G. Tryggvason, A front-tracking method for viscous, incompressible, multi-fluid flows, Journal of Computational Physics 100 (1) (1992) 25–37.
[76] H.S. Udaykumar, R. Mittal, W. Shyy, Computation of solid–liquid phase fronts in the sharp interface limit on fixed grids, Journal of Computational Physics 153 (1999) 534–574.
[77] H.S. Udaykumar, R. Mittal, P. Rampunggoon, A. Khanna, A sharp interface cartesian grid method for simulating flows with complex moving boundaries, Journal of Computational Physics 174 (2001) 345–380.
[78] X. Zhong, A New High-order Immersed Interface Method for Multi-phase Flow, AIAA Paper 2006-1294, 2006.
[79] N.K. Yamaleev, M.H. Carpenter, A systematic methodology for constructing high-order energy stable WENO schemes, Journal of Computational Physics 228 (11) (2009) 4248–4272.
[80] J. Larsson, B. Gustafsson, Stability criteria for hybrid difference methods, Journal of Computational Physics 227 (5) (2008) 2886–2898.
[81] B. Gustafsson, H.-O. Kreiss, A. Sundstrom, Stability theory of difference approximations for mixed initial boundary value problems, II, Mathematics of Computation 26 (119) (1972) 649–686.

[82] M.H. Carpenter, D. Gottlieb, S. Abarbanel, The stability of numerical boundary treatments for compact high-order finite-difference schemes, Journal of Computational Physics 108 (1993) 272–295.
[83] J. Casper, M.H. Carpenter, Computational considerations for the simulation of shock-induced sound, SIAM Journal of Scientific Computing 19 (3) (1998) 813–828.
[84] A. Suresh, Interaction of a shock with a density disturbance via shock fitting, Journal of Computational Physics 206 (2005) 6–15.
[85] C.W. Shu, S. Osher, Efficient implementation of essentially nonoscillatory shock-capturing schemes,II, Journal of Computational Physics 83 (1) (1989) 32–78.
[86] A.R. Kasimov, D.S. Stewart, On the dynamics of self-sustained onedimensional detonations: a numerical study in the shock-attached frame, Physics of Fluids 16 (2004) 3566–3578.
[87] T.J. Poinsot, S.K. Lele, Boundary conditions for direct simulations of compressible viscous flow, Journal of Computational Physics 101 (1) (1992) 104–129.